

***THE DYNAMIC SHAPE FACTOR OF SODIUM CHLORIDE
NANOPARTICLES AS REGULATED BY DRYING RATE***

Z. Wang^{1,2}, S. M. King², E. Freney³, T. Rosenoern², M. Smith², Q. Chen², M. Kuwata²,
E. R. Lewis⁴, U. Pöschl⁵, W. Wang¹, P. R. Buseck³, and S. T. Martin^{2*}

¹ Environment Research Institute, Shandong University, Ji'nan, Shandong, China

² School of Engineering and Applied Sciences & Department of Earth and Planetary Sciences,
Harvard University, Cambridge, MA, USA

³ School of Earth and Space Exploration and Department of Chemistry and Biochemistry, Arizona
State University, Tempe, AZ, USA

⁴ Atmospheric Sciences Division, Brookhaven National Laboratory, Upton, NY, USA

⁵ Max Planck Institute for Chemistry, Biogeochemistry Department, Mainz, Germany

*To Whom Correspondence Should be Addressed: *E-mail: scot_martin@harvard.edu*

March 2010

Submitted to
Aerosol Science & Technology

Environmental Sciences Department/Atmospheric Sciences Division

Brookhaven National Laboratory

P.O. Box 5000

Upton, NY 11973-5000

www.bnl.gov

Notice: This manuscript has been authored by employees of Brookhaven Science Associates, LLC under Contract No. DE-AC02-98CH10886 with the U.S. Department of Energy. The publisher by accepting the manuscript for publication acknowledges that the United States Government retains a non-exclusive, paid-up, irrevocable, world-wide license to publish or reproduce the published form of this manuscript, or allow others to do so, for United States Government purposes.

This preprint is intended for publication in a journal or proceedings. Since changes may be made before publication, it may not be cited or reproduced without the author's permission.

DISCLAIMER

This report was prepared as an account of work sponsored by an agency of the United States Government. Neither the United States Government nor any agency thereof, nor any of their employees, nor any of their contractors, subcontractors, or their employees, makes any warranty, express or implied, or assumes any legal liability or responsibility for the accuracy, completeness, or any third party's use or the results of such use of any information, apparatus, product, or process disclosed, or represents that its use would not infringe privately owned rights. Reference herein to any specific commercial product, process, or service by trade name, trademark, manufacturer, or otherwise, does not necessarily constitute or imply its endorsement, recommendation, or favoring by the United States Government or any agency thereof or its contractors or subcontractors. The views and opinions of authors expressed herein do not necessarily state or reflect those of the United States Government or any agency thereof.

Abstract

The influence of drying rate on the volume-equivalent dynamic shape factor χ of NaCl particles was investigated. The drying rate was controlled in a laminar flow tube by use of a dry outer sheath flow and an inner wet aerosol flow. The drying rate at the efflorescence relative humidity of 45% was varied from 5.5 ± 0.9 to $101 \pm 3 \text{ RH s}^{-1}$, where RH represents one percent unit of relative humidity. Dry particles having mobility diameters of 23 to 84 nm were studied, corresponding to aqueous particles of 37 to 129 nm at 57% RH. At each mobility diameter and drying rate, the critical supersaturation of cloud-condensation activation was also measured. The mobility diameter and the critical supersaturation were combined in an analysis to determine the value of χ , which ranged from 1.02 to 1.26, depending on particle diameter and drying rate. Transmission electron micrographs of collected dry particles showed that the morphologies varied from spheres to cubes. For fixed particle diameter, the determined value of χ decreased with increasing drying rate. For example, it decreased from 1.26 to 1.09 for a shift in drying rate from 5.5 ± 0.9 to $101 \pm 3 \text{ RH s}^{-1}$ for particles having a mass-equivalent dry diameter of 35.7 nm. The results also show that for fixed drying rate there was a maximum in χ located between 35- and 40-nm dry mobility diameter, with a lower χ for both smaller and larger particles. The results of this study, in conjunction with the introduced apparatus for obtaining quantified drying rates, can allow the continued development of a more detailed understanding of the morphology of submicron salt particles, with the potential for the follow-on development of quantitative modeling of evaporation and crystal growth at these dimensions.

1. Introduction

Many instruments classify particles by drag force (Baron and Willeke, 2001a). Examples include the differential mobility analyzer which classifies by electric mobility Z , impactors and cyclones which classify by aerodynamic diameter d_a , and several particle mass spectrometers which classify by vacuum aerodynamic diameter d_{va} . Instrument performance is typically defined for spherical particles, and the instruments include a dynamic shape factor χ in their performance equations to compensate for nonspherical particle geometries. The volume-equivalent dynamic shape factor of an aerosol particle is the ratio of the drag force on it to that on a spherical particle of identical volume (Davies, 1979; Baron and Willeke, 2001b). The factor χ has been defined both on volume-equivalent and mass-equivalent bases (Brockmann and Rader, 1990; DeCarlo et al., 2004). Mass equivalency eliminates internal porosity in constructing the sphere whereas volume equivalency retains that porosity in the sphere. For nonporous particles, the two equivalent diameters are equal. In our application described herein, we follow the conventions described in DeCarlo et al. (2004), and we therefore employ the dynamic shape factor on a volume-equivalency basis.

Various approaches exist for estimating the dynamic shape factor, ranging from calculation for perfect geometries such as cubes (Dahneke, 1973a; b; c) or spherical aggregates (Cheng et al., 1988; Kousaka et al., 1996) to measurement by combinations of techniques (Barbe-le Borgne et al., 1986; Brockmann and Rader, 1990; Baron and Willeke, 2001b; Park et al., 2004; Zelenyuk et al., 2006; Kuwata and Kondo, 2009). In the latter category, estimates of the volume-equivalent diameter can be obtained by microscopy, which can be combined with a measurement of the aerodynamic or mobility diameter to obtain the shape factor (Baron et al.,

2001; Park et al., 2004). Another method for determining the shape factor is to measure separately the mobility and aerodynamic diameters (Katrib et al., 2005).

The dynamic shape factor of a particle is influenced by the conditions of aerosol production and subsequent processing. For example, pyrolytic or evaporative production of aerosol particles of metal oxides or noble metals, optionally followed by further thermal conditioning, can lead to a variety of morphologies (Kodas and Hampden-Smith, 1999). Similarly, soot particles produced by open-flame synthesis, as well as diesel particles emitted by engine combustion, typically have a fractal backbone of black carbon spherules that can be coated by semivolatile organic material (Kittelson, 1998; Park et al., 2004; Slowik et al., 2004; Slowik et al., 2007). The extent and history of the organic coating can influence the dynamic shape factor.

The dynamic shape factor of NaCl aerosol particles having dry mobility diameters less than 100 nm (i.e., nanoparticles) is an important source of uncertainty for the calibration of cloud condensation nuclei counters (CCNCs) (Kreidenweis et al., 2005; Shilling et al., 2007; Rose et al., 2008; Kuwata and Kondo, 2009). Although there is a rich literature on the shapes of much larger particles prepared by spray evaporation of aqueous NaCl and other salts (e.g., the seminal work of Charlesworth and Marshall (1960), many later studies as reviewed in Lewis and Schwartz (2004), and a recent study by Lin and Gentry (2003)), systematic experimental measurements of how the drying rate influences the efflorescence and the morphology of nano-size salt particles have not been described previously. Although particle shape is expected to depend on the size of the particle and the rate of drying (Mikhailov et al., 2004; Biskos et al., 2006a; Rose et al., 2008; Mifflin et al., 2009; Mikhailov et al., 2009), accurate and detailed prediction of particle shape resulting from evaporative drying is challenging because the model

equations must, at a minimum, couple diffusive gas mass transfer, diffusive liquid mass transfer, advancing crystal fronts, and local heating from latent heat release (Duffie and Marshall, 1953; Leong, 1987; Abramzon and Sirignano, 1989; Yun and Kotas, 1993; Walton, 2000; Brenn et al., 2001). Measurements are therefore required.

The absence of definitive χ values for salt nanoparticles is a crucial uncertainty in the calibration of CCNCs because these instruments are calibrated against known salts, commonly sodium chloride and ammonium sulfate, under the assumption that the response to these salts is known (Kreidenweis et al., 2005; Shilling et al., 2007; Rose et al., 2008; Kuwata and Kondo, 2009). Kreidenweis et al. (2005) and Rose et al. (2008) reviewed the problem and showed that calibrations based on different assumed physicochemical properties of salts can give inconsistent results, even for a single instrument in the same research group. One contributing factor to inconsistent calibrations is the variable dynamic shape factor of sodium chloride nanoparticles. Whereas ammonium sulfate crystallizes as spherical or nearly spherical particles for a range of drying rates (Biskos et al., 2006b; Zelenyuk et al., 2006; Kuwata and Kondo, 2009), the different morphologies and hence dynamic shape factors of NaCl particles, as well as their dependence on factors such as drying rate and particle diameter, are not well understood and hardly quantified. Rose et al. (2008), for example, showed that the CCNC was best calibrated using χ of 1.00 for NaCl particles effloresced by rapid mixing with dry air and χ of 1.08 for passage through a diffusion dryer. Even if regular cubes form, χ may vary from 1.08 to 1.24 over the transition from low to high Knudsen numbers (Dahneke, 1973c; Biskos et al., 2006c). There is therefore a need and an interest to understand how the drying rate affects the dynamic shape factor of NaCl particles, with the ultimate goal of advancing the theoretical understanding of the connections among aqueous particle diameter, drying rate, and dry particle morphology.

Achieving controlled and known drying rates is an experimental challenge. One method described in literature is the mixing of a humid aerosol flow with a flow of dry nitrogen or pure air. This approach should lead to rapid drying, but the reproducibility of the technique among laboratories or even among apparatuses within the same laboratory depends on the specific aspects of the mixing tied to the apparatus and its operation. Moreover, the quantification of the drying rate (RH s^{-1}), including a possible heterogeneity of drying rates within the mixed aerosol, is completely uncertain, even the more so if the humid and dry flows are mixed turbulently by baffling or other flow constrictions as is commonly done. Another method is to flow the aerosol through a Nafion tube or through a dessicant dryer. Provided that the flow rates and the geometries are precisely stated, these methods should lead to reproducibility among experimenters, but the quantification of the drying rate, as required for theoretical studies, is still absent, and the ability to vary this rate is limited.

The study described herein addresses the needs expressed above. Specifically, the dynamic shape factor of NaCl aerosol particles having dry mobility diameters less than 100 nm was obtained for a range of quantified drying rates. A laminar-flow tube with a core wet-aerosol flow and an outer dry-air sheath flow was used. The drying rates were quantified on the basis of a diffusion calculation for this optimized geometry and flow regime. The rates were varied by adjusting the initial RH difference between the aerosol and sheath flows. The value of χ of the dry particles was obtained by using a differential mobility analyzer (DMA) to control the mobility diameter $d_{m,+1}^{dry}$ (+1 charge) of the dry particle and by measuring the critical supersaturation S_c for CCN activation of the mobility-classified particles, as described in the next section.

2. Theory for $\chi = f(d_{m,+1}^{dry}, S_c)$

The relationship of $\chi = f(d_{m,+1}^{dry}, S_c)$ is derived, as follows. The dry solute mass m_p^{dry} of a fully water-soluble salt particle is related to the critical supersaturation S_c of CCN activation by the Köhler model of equation 1. The notation $S_c = S[w_t]:\max[f]$ of that equation reads that S_c is defined as the value of S at the point of maximum in the function f for the running variable w_t .

$$S_c = S[w_t]:\max[1+S/100] = \max \left[a_w \exp \left[\frac{4\sigma V_{m,w}}{RT d_{ve}^{aq}} \right] \right] = \max \left[a_w \exp \left[\frac{4\sigma V_{m,w}}{RT \left((6/\pi) (m_p^{dry} / w_t \rho_{aq}) \right)^{1/3}} \right] \right] \quad (1)$$

The terms of equation 1 include percent saturation S , solution water activity a_w , solution surface tension σ , solution partial molar volume of water $V_{m,w}$, universal gas constant R , absolute temperature T , aqueous particle diameter d_{ve}^{aq} , solute weight fraction w_t , and solution density ρ_{aq} . The right-hand side of equation 1 shows that the maximum depends on the independent parameter m_p^{dry} . The other terms a_w , σ , $V_{m,w}$, and ρ_{aq} depend on the running variable w_t . For these terms, the “AIM-based activity parameterization (AP3)” model of Rose et al. (2008) provides the relations we use. The AP3 model and the *AerosolCalculator* also used in this study (www.seas.harvard.edu/AerosolCalculator) have similar embedded thermodynamic values and give similar results.

Equation 1 is solved by us for multiple values of m_p^{dry} to obtain S_c . From a resulting lookup table of $\{S_c, m_p^{dry}\}$, we construct a parameterization $m_p^{dry}[S_c]$ for $0.1\% < S_c < 2.0\%$:

$$m_p^{dry} = \frac{c_0}{S_c^2} \left(1 + c_1 \sqrt{S_c} + c_2 S_c \right) \quad (2)$$

The coefficients c_i are listed in Table 1 for sodium chloride and ammonium sulfate. The form of equation 2 is based on $m_p^{dry} \propto 1/S_c^2$ for an infinitely dilute ideal solution, with an expected

correction term of $\sqrt{S_c}$ for nonideal solutions as described in equation A22 of Lewis (2008) and an additional empirical linear correction term of S_c .

The value of χ is obtained from the following relationship (cf. equation 25 of DeCarlo et al. (2004)):

$$\frac{C_c [d_{m,+1}^{dry}]}{d_{m,+1}^{dry}} = \frac{C_c [d_{ve}^{dry}]}{\chi d_{ve}^{dry}} = \frac{C_c \left[\delta \left((6/\pi) (m_p^{dry} [S_c] / \rho_{dry}) \right)^{1/3} \right]}{\chi \delta \left((6/\pi) (m_p^{dry} [S_c] / \rho_{dry}) \right)^{1/3}} \quad (3)$$

where C_c is the Cunningham slip correction factor (Allen and Raabe, 1985), ρ_{dry} is the dry material density, and δ is the porosity factor of the dry particle that satisfies $d_{ve}^{dry} = \delta d_{me}^{dry}$ for a volume-equivalent diameter d_{ve} and a mass-equivalent diameter d_{me} of the dry particle. For a nonporous particle, $\delta = 1$; for a porous particle, $\delta > 1$. The analysis herein assumes that $\delta = 1$ unless stated otherwise. Equation 3 shows that the value of S_c , in combination with the mobility diameter $d_{m,+1}^{dry}$ classified using the DMA, is sufficient to obtain χ of nonporous NaCl particles, thereby defining the relationship of $\chi = f(d_{m,+1}^{dry}, S_c)$.

For comparison, several studies in the literature have employed a hygroscopic tandem differential mobility analyzer (HTDMA) to obtain the dynamic shape factor (Kramer et al., 2000; Mikhailov et al., 2004; Biskos et al., 2006c). In this technique, the dry mobility diameter $d_{m,+1}^{dry}$ of a salt particle and the mobility diameter $d_{m,+1}^{aq} [RH]$ of its aqueous counterpart at elevated relative humidity are measured. At a fixed RH, there is a one-to-one relationship between the dry solute mass m_p^{dry} of a fully soluble salt particle and the mobility diameter of its deliquesced aqueous counterpart, which we represent by the function $m_p^{dry} [d_{m,+1}^{aq}; RH]$. This relationship depends on the surface tension of the air-solution interface, the partial molar volume of water of

the aqueous solution, the density of the aqueous solution, and the salt hygroscopicity (cf. equations 2a and 3 in Biskos et al. (2006c)). The relationship does not depend on the dynamic shape factor χ or the porosity factor δ of the dry salt particle. The relationship for an HTDMA instrument, which measures $d_{m,+1}^{dry}$, RH, and $d_{m,+1}^{aq}$ can then written as follows:

$$\frac{C_c [d_{m,+1}^{dry}]}{d_{m,+1}^{dry}} = \frac{C_c [d_{ve}^{dry}]}{\chi d_{ve}^{dry}} = \frac{C_c \left[\delta \left((6/\pi) \left(m_p^{dry} [d_{m,+1}^{aq}; \text{RH}] / \rho_{dry} \right) \right)^{1/3} \right]}{\chi \delta \left((6/\pi) \left(m_p^{dry} [d_{m,+1}^{aq}; \text{RH}] / \rho_{dry} \right) \right)^{1/3}} \quad (4)$$

Equation 3 for the DMA-CCNC and equation 4 for the HTDMA differ only in the primary measurement that is used to obtain m_p^{dry} , which is a measurement of S_c in the former and of $d_{m,+1}^{aq}$ in the latter.

3. Experimental

The experimental strategy was to use a differential mobility analyzer (DMA) to select particles of mobility diameter $d_{m,+1}^{dry}$ and to use a CCNC to measure the activated fraction F_a at different setpoint supersaturations. This measurement was repeated at fixed supersaturation for multiple mobility diameters, and a CCN activation curve was thereby obtained. A schematic diagram of the experimental apparatus is shown in Figure 1. The following sections present the method of aerosol generation and preconditioning (§3.1), the design and operation of the horizontal laminar-flow tube (§3.2), the measurement of the CCN activation curve (§3.3), the collection of transmission electron micrographs (§3.4), and the calculation of the drying rate (§3.5).

3.1 Aerosol generation and preconditioning

Polydisperse sodium chloride particles were aerosolized in pure air from aqueous solution (0.1 g L^{-1}) by use of an atomizer (TSI Model 3076) (Liu and Lee, 1975). The humid

aerosol flowed at 3 L min^{-1} through a Nafion conditioner (Permapure Model PD-50T) (Dick et al., 1995), in which the aerosol RH was adjusted to $57 \pm 2\%$. The experiments were performed at room temperature ($298 \pm 1\text{K}$). Under these conditions, the particles remained aqueous. A sensor mounted downstream of the conditioner verified the aerosol RH. As illustrated in Figure 1A, the RH in the drive flow of the Nafion conditioner was adjusted to 57% by use of two mass flow controllers to mix proportioned flows of dry air and air near water saturation. The latter was produced by bubbling pure air through water ($18.3 \text{ M}\Omega \text{ cm}$) in a glass bubbler.

3.2 Aerosol laminar-flow tube

As depicted in Figure 1B, the aerosol of polydisperse particles passed longitudinally as a core flow (0.8 L min^{-1}) within a sheath flow (11.2 L min^{-1}). Linear velocities of the two flows were the same, and laminar conditions were obtained, implying that water vapor was exchanged only by radial diffusion between the aerosol and the sheath volumes. The Pyrex flow tube was 1.2 m long and 4.5 cm (ID) in diameter. The injector for the aerosol flow (1.16 cm ID) was inserted 70 cm into the flow tube, thus allowing sufficient distance for the sheath flow to establish its steady-state flow profile. A collector (1.16 cm ID) of the aerosol flow was inserted 10 cm from the exit of the flow tube. The sheath and aerosol flows were thus exposed to one another for 40 cm, which was equivalent to 3.2 s for the flow rates used. Two flow-smoothing screens (700 mesh) were mounted in the sheath flow to maintain laminar flow, one located just prior to the point of aerosol injection and the other just after the point of aerosol collection. A red laser was used to confirm laminar flow by observing that the particles remained within the core volume along the length of the flow tube. The aerosol and sheath flows were regularly calibrated using Gilibrator bubble flow meters.

The RH of the sheath inflow was conditioned between 6 and 40% (depending on the desired drying rate; cf. Table 2) by the use of proportionate mixing of humid and dry flows. The radial diffusion of water vapor from the aerosol to the sheath volume steadily reduced the aerosol RH along the longitudinal axis of the flow tube. When the RH of the aerosol flow dropped below the efflorescence relative humidity (ERH), the sodium chloride particles crystallized. Biskos et al. (2006a) showed that the ERH for NaCl particles having diameters of 20 nm and larger was 45%. The RH of the aerosol flow exiting the tube was monitored to verify that the value expected from calculation was obtained. Depending on the experiment (cf. Table 2), this RH was between 11 and 41% RH.

The aerosol flow was controlled downstream by the flow controllers installed in a condensation particle counter (CPC; TSI Model 3025; 0.3 L min^{-1}) and in a cloud condensation nuclei counter (Droplet Measurement Technologies, DMT Model CCN-2; 0.5 L min^{-1}) (Roberts and Nenes, 2005; Lance et al., 2006; Rose et al., 2008). The balanced, recirculating sheath flow was controlled using the setup described in Biskos et al. (2006b). Elements are depicted in the right-hand side of Figure 1A. A compressive blower (Minispiral Model SE12RE21SA) aspirated the sheath flow from the flow tube and blew it through a hydrophobic filter (Whatman Model 6702-7500) to remove any aerosol particles. The blower slightly increased the flow temperature, and a heat exchanger (Lytron Model C-HX-4105G1SB) was used to re-equilibrate the flow temperature. The air then passed through a laminar flow element (Furness Controls Model FCO96-20) having a pressure transducer (Aschroft Model CXLdp) mounted to it. Using the pressure drop across the laminar flow elements as its control signal, a proportional-integral-derivative (PID) circuit (Omega Model CN16D52-C24-DC) regulated the blower power and hence the flow rate, providing a feedback-controlled continuous sheath flow.

The flow passed through a Nafion conditioner for adjustment to the desired RH before recirculation into the flow tube.

3.3 CCN Activation Curve

The dried aerosol of polydisperse particles exiting the flow tube passed through a ^{210}Po bipolar charger (NRD Model P-2031) to establish an equilibrium charge distribution on the particles. The aerosol flow then passed through a nano differential mobility analyzer (nDMA, TSI Model 3085) set to select a monodisperse mobility diameter (+1 charge). Flow rates of 0.8 L min^{-1} for the aerosol and 8 L min^{-1} for the sheath were used. The RH of the sheath flow was maintained at 6% to avoid any shape reconstruction of particles inside nDMA. The flow of monodisperse aerosol particles was split into two subflows, the first (0.3 L min^{-1}) entering an ultrafine CPC and the second (0.5 L min^{-1}) entering a continuous-flow CCNC.

Inside the CCNC those particles having a sufficiently large solute mass activated at the set supersaturation (controlled by a temperature gradient in the instrument (Roberts and Nenes, 2005)) to grow into droplets having diameters greater than one micrometer, which were detected by an optical particle counter. Supersaturations from 0.15 to 1.0% were investigated stepwise. The activated fraction at a set supersaturation and mobility diameter was determined as the ratio of the activated particle number concentration detected by the CCNC to the total particle number concentration detected by the CPC. During the experiments, the mobility diameter of the nDMA was scanned from 15 to 90 nm in steps of 2 to 5 nm for each supersaturation, and an activation curve over mobility diameter was thereby obtained. Each activation curve was fit with a sigmoid function, including a filter to omit the effect of multiply charged particles (King et al., 2007). The mobility-equivalent critical dry diameter (used in the left-hand side of equation 3) was taken at $F_a = 0.5$. Raw data are plotted in Figure S1. For comparison, methods based on the sum of two

cumulative Gaussian distribution functions (Rose et al., 2008) and on an inversion to take into account the DMA transfer function (Petters et al., 2007) were also used to analyze the data. Within experimental uncertainty, the three analyses yielded identical critical diameters. The dynamic shape factor was obtained from equation 3.

Calibration of the supersaturation of the CCNC was performed using $(\text{NH}_4)_2\text{SO}_4$ particles for temperature gradients from 3.9 to 17.4 K (Shilling et al., 2007). The $(\text{NH}_4)_2\text{SO}_4$ particles were prepared by nebulization of aqueous solutions. They were dried by dilution with particle-free dry air, followed by further drying in diffusion dryers. The studies in the literature concerning $(\text{NH}_4)_2\text{SO}_4$ particles converge on a dynamic shape factor of 1.02 ± 0.02 for a broad range of diameters and drying methods (Biskos et al., 2006b; Zelenyuk et al., 2006; Rose et al., 2008; Kuwata and Kondo, 2009). Our CCNC calibration using $(\text{NH}_4)_2\text{SO}_4$ particles was based on $\chi = 1.02$, $\delta = 1$, and the “AIM-based activity parameterization (AP3)” model of Rose et al. (2008), using the relations for water activity, surface tension, and density described therein. Equation 2 provides the parameterization of $m_p^{dry} [S_c]$, and its inverse $S_c [m_p^{dry}]$ was used in the calibration.

3.4 Transmission Electron Microscopy

Dried particles were collected by redirecting the outflow from the nDMA (Figure 1) to a nanoparticle electrostatic precipitator (TSI model 3089) (Dixkens and Fissan, 1999). The precipitator, which was operated at a flow rate of 0.8 L min^{-1} and a collection voltage of 10 kV, collected positively charged particles for 30 min onto grids (Ted Pella Inc #1890; lacey-carbon Type-A, 300-mesh copper) for transmission electron microscopy (TEM). From collection through analysis, the ambient relative humidity was closely monitored and never exceeded 30%. This quality-assurance step was required because sodium chloride particles can reconstruct and

change shape when water layers condense, even for RH values significantly below the deliquescence relative humidity (Kramer et al., 2000; Biskos et al., 2006a). The samples were maintained in airtight containers until the time of imaging. The relative humidity in the TEM laboratory was between 8 and 18% during all experiments, and the absolute humidity inside the microscope corresponded to vacuum conditions. TEM images were obtained using a Philips CM200 transmission electron microscope operated at 200 kV. A low-intensity electron beam was used to minimize any changes to the particles during imaging (Wise et al., 2005).

3.5 Drying Rate

The geometry of the apparatus and its operation as relevant to the calculation of drying rate are depicted in Figure 2. For our experimental conditions, the Reynolds number of the flow in the tube was 370, corresponding to laminar motion. An inner core of wet aerosol particles flowing along the central longitudinal axis was surrounded by a dry outer sheath flow. For this setup, the dominant mechanism for water-vapor movement in the radial coordinate was diffusion, as described by Fick's law.

A quantitative model of these processes can be developed for the cylindrical geometry of the flow tube. In any infinitesimal cylindrical volume element at longitudinal coordinate z , radial coordinate r , and azimuthal coordinate θ (Figure 2B), the general mass balance for water combined with Fick's law for diffusion is as follows (Cussler, 1984):

$$\frac{C_0}{100} \left(\frac{\partial RH}{\partial t} + v_r \frac{\partial RH}{\partial r} + \frac{v_\theta}{r} \frac{\partial RH}{\partial \theta} + v_z \frac{\partial RH}{\partial z} \right) = \frac{C_0 D}{100} \left[\frac{1}{r} \frac{\partial}{\partial r} \left(r \frac{\partial RH}{\partial r} \right) + \frac{1}{r^2} \frac{\partial^2 RH}{\partial \theta^2} + \frac{\partial^2 RH}{\partial z^2} \right] \quad (5)$$

where t is time, C_0 is the vapor concentration of pure water, RH is the relative humidity, v_i is the advective flow velocity in direction i , and D is the diffusion coefficient of water in air.

Conditions for the modeling include incompressible flow and constant temperature.

For our experimental conditions, there is advection among volume elements only in z , implying $v_r = v_\theta = 0$ and that $z = v_z t$. There is also azimuthal symmetry among the elements, meaning that $\partial/\partial\theta$ between elements is zero. Longitudinal diffusion among the elements (represented by $\partial^2 RH/\partial z^2$) is negligible for the residence time of our experimental setup. We seek the solution at steady state, and we can therefore omit terms of $\partial/\partial t$. The general governing differential equation (i.e., equation 5) therefore reduces to the specific equation that must be satisfied by all volume elements in our experimental setup:

$$v_z \frac{\partial RH}{\partial z} = \frac{D}{r} \frac{\partial}{\partial r} \left(r \frac{\partial RH}{\partial r} \right) \quad (6)$$

The experimental setup imposes several boundary conditions for the solution of equation 6. For $RH(r, z)$, the conditions to satisfy are $RH(r < r_{aerosolFlow}, 0) = RH_{0,aerosolFlow}$, $RH(r_{aerosolFlow} < r < r_{sheathFlow}, 0) = RH_{0,sheathFlow}$, $(\partial RH/\partial r)_{r=0} = 0$ for all z , and $(\partial RH/\partial r)_{r=r_{sheathFlow}} = 0$ for all z , where $RH_{0,aerosolFlow}$ and $RH_{0,sheathFlow}$ are the initial relative humidity in the inner and outer tubes, respectively, and the two flows come into first contact at $z = 0$.

The analytical solution of equation 6 for the stated boundary conditions and an approximation of a flat-flow profile is an infinite expansion, as follows:

$$\begin{aligned} RH(r, z) = & \left[1 - \left(\frac{r_{aerosolFlow}}{r_{sheathFlow}} \right)^2 \right] RH_{sheathFlow} + \left(\frac{r_{aerosolFlow}}{r_{sheathFlow}} \right)^2 RH_{aerosolFlow} \\ & + 2 \left(\frac{r_{aerosolFlow}}{r_{sheathFlow}} \right) (RH_{aerosolFlow} - RH_{sheathFlow}) \times \\ & \left[\sum_{n=1}^{\infty} \frac{J_1 \left(\alpha_n \frac{r_{aerosolFlow}}{r_{sheathFlow}} \right)}{\alpha_n (J_0(\alpha_n))^2} J_0 \left(\alpha_n \frac{r}{r_{sheathFlow}} \right) e^{\frac{-z}{z_n}} \right] \end{aligned} \quad (7)$$

301 where J_0 and J_1 are Bessel functions of the first kind and $z_n = (r_{sheathFlow}^2 v_z) / (D \alpha_n^2)$. The
 302 expansion is in the roots α_n of $J'_0(\alpha_n) = 0$ (i.e., there is an infinite set of progressive roots). The
 303 first several of these roots are 3.8, 7.0, and 10.2, and they asymptotically approach $(n + 1/4) \pi$.
 304 The first term of equation 7 is the RH at long distance; the second term represents the evolution
 305 of RH from short to long distances. The evolution with distance is controlled by the decay
 306 constants z_n of the individual modes, the first several of which are 0.17, 0.051, and 0.024 m for
 307 the parameters of our experiment. The implication is that by approximately 0.1 m only the first
 308 few terms of equation 7 contribute appreciably to $RH(r, z)$.

309 Modeling results are summarized in Tables 2 and 3 as well as Figures 2C and 2D.

310 Parameter values for the modeling include $v_z = 0.127 \text{ m s}^{-1}$, $D = 2.56 \times 10^{-5} \text{ m}^2 \text{ s}^{-1}$, $r_{aerosolFlow} =$
 311 $5.8 \times 10^{-3} \text{ m}$, and $r_{sheathFlow} = 2.25 \times 10^{-2} \text{ m}$. The values of $RH_{0,sheathFlow}$ and $RH_{0,aerosolFlow}$ are
 312 listed in the tables. The analytical solutions obtained by equation 7 were compared to numerical
 313 solutions, and the agreement between the two approaches was good.

314 For our study, the key modeling endpoint is the drying rate at the longitudinal position at
 315 which particles crystallize. We calculate an average drying rate RH'_{ERH} in the aerosol flow at
 316 the efflorescence relative humidity, as follows:

$$317 \quad RH'_{ERH} = \left(\frac{dRH}{dt} \right)_{ERH} = \frac{v_z \int_0^{r_{inner}} r \left(\frac{\partial RH}{\partial z} \right)_{ERH, r} dr}{\int_0^{r_{inner}} r dr} \quad (8)$$

318 where $(\partial RH / \partial z)_{ERH, r}$ is evaluated at the position r that satisfies $RH(r, z) = ERH$. Table 2 lists

319 RH'_{ERH} for the four different experimental conditions of this study.

In regard to the approximation of a flat-flow profile, the actual profile should approach parabolic by the end of the tube. Treatment of the flow transition, however, is not within the scope of our study. Nevertheless, the correction for a full treatment to the rate of radial diffusion of water vapor (i.e., drying rate) should be minor compared to the larger stepwise changes that occur for the different settings of the initial RH values in the inner and outer tubes (i.e., Table 3).

4. Results

4.1 Drying Rates

The results of model cases I through IV for different initial conditions of $RH_{0,sheathFlow}$ and $RH_{0,aerosolFlow}$ are presented in Table 3. The associated RH profiles are illustrated in Figure 2C by four lines, each representing the radially averaged $RH_{aerosolFlow}(t; t = z/v_z)$ of one of the model cases. As expected, $RH_{aerosolFlow}$ decreases sharply at the beginning of the diffusive exchange with the drier air of $RH_{0,sheathFlow}$, and the highest instantaneous drying rates in the aerosol flow are obtained at time zero (cf. Table 3). Full homogenization between the aerosol and sheath flows is largely obtained in all four cases. The drying rates correspondingly decrease for increasing interaction time until falling to zero after full homogenization.

The average drying rate RH'_{ERH} at efflorescence is given by the slope of $RH_{aerosolFlow}(t)$ at ERH. In Figure 2C, the intersections of the four lines for $RH_{aerosolFlow}(t)$ with the inset horizontal line determine those time points. In Figure 2D, values of RH'_{ERH} as calculated by equation 8 are represented by lines of constant ΔRH for increasing $RH_{0,aerosolFlow}$, where $\Delta RH = (RH_{0,aerosolFlow} - RH_{0,sheathFlow})$. Values of RH'_{ERH} for the model cases I to IV (i.e., the slopes of Figure 2C) are represented by the filled triangles along the lines. The results represented in Figure 2D indicate that the same value of RH'_{ERH} can be obtained with different combinations of conditions. For example, all four lines pass through a drying rate of 40 RH s^{-1} . Figure 2D also

shows that, with ΔRH fixed, RH'_{ERH} decreases for increasing $RH_{0,aerosolFlow}$. In comparison, with $RH_{0,aerosolFlow}$ fixed, RH'_{ERH} increases for increasing ΔRH . Open circles in Figure 2D show RH'_{ERH} for experiments 1 through 4 of this study, as summarized in Table 2. The rates range from 5.5 ± 0.9 to 101 ± 3 RH s⁻¹ for these experiments.

4.2 Dynamic shape factor of NaCl particles

Figure 3 shows the transmission electron micrographs of particles collected for the fastest and slowest drying rates studied (i.e., experiments 1 and 4 of Table 2). The three rows in Figure 3 show particles collected for dry mobility diameters of 25, 40, and 65 nm, respectively. Drying in all three cases was initiated from aqueous particles of 57% RH, corresponding to initial aqueous diameters of 36 to 39, 58 to 63, and 95 to 102 nm, respectively, as calculated using the *AerosolCalculator*, for dynamic shape factors of the dry particles of 1.08 to 1.24. The images show that the particles tended toward sharper edges when dried slowly and softer edges when dried rapidly. The shapes of the particles were quantitatively characterized by descriptors of aspect ratio, form factor, and roundness, using the definitions of each of these as given in Hentschel and Page (2003). The average values of the shape descriptors are listed in Table 4. For all particle sizes, the descriptors are closer to unity for fast drying rate, indicating more spherical particles at fast compared to slow drying. Although this trend is generally well known qualitatively, our present work provides quantitative results that fast and slow drying correspond, respectively, to 101 ± 3 and 5.5 ± 0.9 RH s⁻¹ for the particle sizes studied. The variability in the images confirms that the morphologies and hence the dynamic shape factors of NaCl particles are influenced by both drying rate and particle size.

CCN activation curves, which represent the activated particle fraction for increasing mobility diameter, are shown in Figure 4 for NaCl particles prepared by drying aqueous particles

at different rates and exposed to 0.5% supersaturation. Compared to the mass-equivalent diameter of 35.7 nm expected at this supersaturation, the measured mobility-equivalent critical diameters (i.e., the mobility diameter at 50% activated fraction) were higher, indicating nonspherical particles. For comparison, arrows in the figure mark the mobility-equivalent critical diameters expected for particles having χ of 1.00 (i.e., a sphere), of 1.08 (i.e., a cube in the continuum regime), and of 1.24 (i.e., a cube in the free-molecule regime) (DeCarlo et al., 2004; Biskos et al., 2006c). The measured activation curves straddle these values, with higher χ for slower RH'_{ERH} . The precise dynamic shape factors associated with the curves were obtained using equation 3. The values of χ are 1.26, 1.18, 1.15, and 1.09 for values of RH'_{ERH} of 5.5 ± 0.9 , 29.7 ± 0.7 , 58.4 ± 0.9 , and 101 ± 3 RH s⁻¹, respectively. The steepness of the activation curves are also equivalent to that of the calibration (cf. Figure S2), indicating homogeneity in the shape factor among different NaCl particles in the aerosol.

For each drying rate, activation curves were collected for supersaturations ranging from 0.15 to 1.0%. Figure 5 shows the results obtained for RH'_{ERH} of 29.7 ± 0.7 RH s⁻¹. For orientation, the thick solid lines in Figures 4 and 5 represent the same data. By use of the approach described for the data of Figure 4, shape factors were obtained for the mobility-equivalent critical diameters of Figure 5. These shape factors for RH'_{ERH} of 29.7 ± 0.7 RH s⁻¹ are plotted in Figure 6 as the black circles. The other shape factors in Figure 6 were obtained from plots analogous to those of Figure 5 but for other drying rates. Selected size-dependent shape factors of Figure 6 are plotted for a complementary view in Figure 7 as drying-rate-dependent shape factors.

The sensitivity of the values of χ shown in Figures 6 and 7 to assumptions and uncertainties in the analyses can be considered. For example, a value of χ of 1.02 was used by us

for the $(\text{NH}_4)_2\text{SO}_4$ particles in the calibration of S_c for the CCNC. Although this value is recommended, some previous work has suggested that the χ value of small $(\text{NH}_4)_2\text{SO}_4$ particles can vary between 1.00 and 1.04 (Biskos et al., 2006b; Zelenyuk et al., 2006; Rose et al., 2008; Kuwata and Kondo, 2009). CCNC calibration with these values correspondingly shifts our determined values of χ for NaCl particles lower or higher by 0.02. Regarding the porosity factor, our analysis assumed a δ value of 1. Equation 3 shows that the term $\chi\delta$ is lumped together, with a small additional correction in the numerator within the C_c term. The result is that an increase of δ to 1.01 shifts the χ value down by 0.02. The activation temperature within the CCNC, which compared to ambient is warmer by an unknown value of the order 3 to 6 K, represents another potential uncertainty because the calibration is influenced by temperature (cf. equation 1) (Rose et al., 2008). For this reason, Table 1 includes calibration at 298 and 304 K. Nevertheless, there is high co-variance between NaCl and $(\text{NH}_4)_2\text{SO}_4$ particles for the temperature sensitivity of the CCNC response, with the net result that there is a negligible influence on χ ($<10^{-4}$) from temperature uncertainty. Although the combined uncertainties outlined in this paragraph can possibly systematically shift the quantitative values we report for χ of the NaCl particles, the qualitative trends with drying rate that we report are robust: (1) there is a maximum in the shape factor at 35 to 40 nm that falls off to smaller and larger diameters and (2) the shape factor decreases with faster drying rate.

5. Discussion

For NaCl particles in their idealized habit of cubes, the line χ_t^{cube} of Figure 6 shows the expected value of the shape factor (i.e., corresponding to the size-dependent shape factor in the transition regime of the Knudsen number). In comparison, the actual measurements of the shape factors are largely bracketed by the values expected for a sphere (i.e., 1.00) and a cube (i.e.,

χ_t^{cube}). Particles having shape factors less than χ_t^{cube} are progressively more spherical than cubic.

As clearly illustrated in Figure 6 and Figure 7, the dynamic shape factor of NaCl particles is a function of drying rate (§5.1) as well as particle size (§5.2).

5.1 Dependence of χ on drying rate

Extremes of drying rate and the associated effects on the morphology of crystallized particles can be considered (Duffie and Marshall, 1953; Leong, 1987; Abramzon and Sirignano, 1989; Yun and Kodas, 1993; Walton, 2000; Brenn et al., 2001). Key concepts are (1) that the development of a morphology implies the diffusive movement of NaCl monomers and (2) that the diffusive movement of these monomers is facilitated by the water content of the particle. At one extreme of sufficiently rapid drying, water evaporation and hence removal from the particle is faster than NaCl monomers can move. In this case, the crystallizing solute does not have enough time to form a euohedral crystal, and the dry particles are locked into a morphology having rounded edges, approaching in a limit those of a sphere. At the other extreme of sufficiently slow drying, water removal is slower than the movement of NaCl monomers, and there is sufficient time for a local or global minimum of the Wulff shape to form on crystallization, corresponding to a cube in the case of NaCl (Adamson and Gast, 1997).

For the experiments conducted herein, unknown a priori is whether the employed drying rates covered a sufficient range to approach either or both of the aforementioned extremes. However, the observations can be an a posteriori guide. Figure 7 shows that the range of drying rates employed (i.e., 5.5 ± 0.9 to 101 ± 3 RH s⁻¹) progressively decreases the value of the shape factor, in agreement with the general principles set out above. For particles having mass-equivalent dry diameters of 35.7 nm, the derived shape factor decreases from 1.26 for 5.5 ± 0.9 RH s⁻¹ to 1.09 for 101 ± 3 RH s⁻¹, indicating the transition from a cubic to a more

spherical particle. Therefore, for this diameter, one extreme of fully sufficient slow drying was obtained for $5.5 \pm 0.9 \text{ RH s}^{-1}$. Drying rates faster than $101 \pm 3 \text{ RH s}^{-1}$, however, are required to achieve the other extreme of sufficiently fast to form perfect spheres. These results of inferred geometrical shape from the dynamic shape factor (i.e., cubes to spheres with increasing drying rate) are supported by the images shown in Figure 3 for the 40-nm particles. Figure 7 also shows, however, that for other particle sizes, a drying rate of $5.5 \pm 0.9 \text{ RH s}^{-1}$ was insufficient to reach the extreme of sufficiently slow drying. For example, particles toward either limit of the size range studied (e.g., 22.7 and 65.2 nm in Figure 7) had shape factors of 1.13 at the slowest drying rate studied, indicating that they were far from cubic and that drying rates slower than $5.5 \pm 0.9 \text{ RH s}^{-1}$ are needed to reach the extreme of sufficiently slow drying.

5.2 Dependence of χ on particle size

The dependence of the dynamic shape factor on particle size is shown in Figure 6 for different drying rates. The dynamic shape factor at all drying rates has a maximum value for a dry mobility diameter of 35 to 40 nm, falling off to lower values both for smaller and larger particles. For example, with a drying rate of $5.5 \pm 0.9 \text{ RH s}^{-1}$, the maximum χ of 1.26 is observed around 40 nm, and decreases to 1.15 at 24 nm and 1.11 at 84 nm.

The key concepts introduced above can provide a qualitative explanation of the trend in dynamic shape factor with particle size. For particles sufficiently small, particle-phase diffusion of water to the surface of the evaporating particles has a small characteristic time, and all water can be removed almost immediately in a flash vaporization, shutting down the water-lubricated mobility μ of NaCl monomers along surfaces that is required to form euohedral shapes. The characteristic time of diffusive movement of monomers scales as L^2/D , where L is the length scale and D is the surface diffusion coefficient of NaCl monomers, which is proportional by the

Einstein relation to their mobility μ . As a result of the flash vaporization, the time available for diffusive movement of NaCl monomers is short and insufficient for full euhedral growth as a cube. For progressively larger particles, the dominance of this timescale decreases because of the increasing characteristic time of particle-phase diffusion of water. At the other end of the size domain, however, for particles sufficiently large, the characteristic time given by L^2/D increases because the absolute length L that NaCl monomers must diffuse to transform a sphere into a cube increases. For particles represented by sufficiently large L , the characteristic time for particle-phase diffusion of water is shorter than that of euhedral growth, again resulting in particles that have at least partially spherical morphology. The combination of these two effects, one favoring more spherical particles at the small end of the size range and the other more spherical particles at the large end of the size range, can qualitatively explain the appearance of a maximum in the dynamic shape factor (i.e., indicative of more cubic particles) at an intermediate diameter for all drying rates (Figure 6).

5.3 Comparison to literature

Drying methods employed in previous studies of the dynamic shape factor of NaCl particles include (1) the mixing of the humid aerosol with dry air flow or (2) the passage of the aerosol through a dessicant-based diffusion dryer or a Nafion conditioner. Previous studies, including their methods of drying, the particle size ranges employed, and the reported shape factors, are summarized in Table 5. These studies did not estimate the drying rate (i.e., RH s^{-1}) associated with their observations. Most of the studies also reported the final dry diameter rather than the initial aqueous diameter (i.e., this diameter is expected to be the controlling factor, in conjunction with the drying rate).

Kelly and McMurry (1992) used measurements of mobility and aerodynamic diameters to obtain effective densities of 120- to 560-nm NaCl particles. The particles were produced by atomizing NaCl solutions and dried using a diffusion dryer. The mobility diameter was selected using a DMA. Impactor stages were used to classify the aerodynamic diameter at just four cut points, implying a low resolution and meaning that the constraints on the inferred shape factor were comparatively weak. A shape factor of 1.08 reconciled the effective density within 8% to the known material density, and 8% was considered well within the uncertainty of the weak constraints.

Kramer et al. (2000) used an HTDMA to study the dynamic shape factor of atomized NaCl particles. A dessicant-based diffusion dryer was used to effloresce the particles. The Cinkotai-model of hygroscopicity described in Kramer et al. (2000) yielded $\chi = 1.17$ for dry particles of 96-nm mobility diameter. In a data reanalysis carried out by us using the *AerosolCalculator* yields $\chi = 1.19$ (i.e., 96-nm dry particles and 162.6-nm aqueous particles at 75% RH). Kramer et al. (2000) did not provide sufficient detail concerning the dryer geometry to allow us to estimate the drying rate.

Mikhailov et al. (2004) using HTDMA measurements reported χ of 1.06 and 1.07 for particles having dry mobility diameters of 99 and 201 nm, respectively. A silica gel diffusion drier (50 cm length, 1-cm inner diameter, 10-cm outer diameter, 1 L min⁻¹ flow) was employed to dry the aqueous particles. Using equation 8 and an assumed initial aerosol RH of 95%, we estimate the drying rate for the study of Mikhailov et al. (2004) as 68% RH s⁻¹ at efflorescence. For conditions in our study most proximate to those of Mikhailov et al. (2004) (i.e., drying rate of 58.4 ± 0.9 RH s⁻¹ and extrapolation of the trend from 82- to 100- nm particles (cf. Figure 6)), we obtain a value of $\chi = 1.07$, which is in good agreement with that of Mikhailov et al. (2004).

Based on HTDMA data, Biskos et al. (2006c) reported values for χ of 1.22 to 1.24 for NaCl particles of 6- to 60-nm dry mobility diameter. In one set of experiments, aerosol particles were formed by vaporizing and condensing granular NaCl. Prior to the HTDMA measurements, these particles were deliquesced and effloresced in a conditioning cycle in a Nafion tube (Perma Pure Model MD-110, 0.2 cm ID of inner tube, 0.6 cm ID of outer tube; initial aerosol RH of 95%; 1 L min⁻¹ aerosol flow). Using equation 8, we estimate a drying rate of 1700 RH s⁻¹ at efflorescence. In another set of experiments, a high-purity NaCl aqueous solution was electrosprayed to generate an aerosol. The primary droplets from the tip of the capillary were diluted with 1 L min⁻¹ filtered dry air, resulting in rapid drying to below 5% RH. On the basis of Figures 6 and 7, the fast drying rates of both sets of experiments are anticipated to yield values of χ close to 1, yet the data of Biskos et al. (2006c) correspond to values of 1.22 to 1.24. This discrepancy cannot be fully explained at this time. In this regard, future experiments are highly warranted in which an aerosol of dry NaCl particles is divided into two flows for parallel analysis by HTDMA and DMA-CCNC apparatus. If, on the one hand, similar values of χ are obtained in the parallel measurements, then we can conclude that the drying methods of Biskos et al. (2006c), which were not a focus of that study, should be examined more closely to understand how particles having values of χ in the cubic regime formed. If, on the other hand, the values of χ from the two methods remain dissimilar when conducted in parallel, then a close look at the parameterizations in the analysis must be considered, including possibilities that the equations of surface tension, partial molar volume of water, density of the aqueous solution, and salt hygroscopicity are not accurate in one or both of the super- or subsaturated regimes.

For 100- to 300-nm dry NaCl particles, Zelenyuk et al. (2006) studied the effect of particle shape on the relationship between mobility and vacuum aerodynamic diameters. Those

authors concluded that nearly spherical dry NaCl particles were produced from rapid drying (i.e., mixing wet and dry flows directly at a ratio of 1:50) whereas cubic NaCl particles were formed by slow drying with diffusion dryers. Although the particle sizes studied by Zelenyuk et al. (2006) were larger than those of our study, their results nevertheless support the same trends as ours showing the dependence of χ on drying rate. For the “slow drying” conditions of Zelenyuk et al. (2006), we estimate a drying rate of 45 RH s⁻¹ at efflorescence, with possible variation range of 30 to 60 RH s⁻¹ for the employed diffusion dryer (TSI Model 3062). Zelenyuk et al. (2006) also studied even larger particles of 200 to 800 nm and observed a trend of χ from 1.06 to 1.17 as particle size increased.

Rose et al. (2008) performed CCNC calibration experiments with both (NH₄)₂SO₄ and NaCl particles of 20- to 220-nm dry mobility diameter. The particles were generated by atomizing aqueous salt solutions. In one set of experiments, the particles were dried by rapid dilution with air to below 15% RH. The cross-calibration between (NH₄)₂SO₄ and NaCl particles was good for χ = 1.00 using the same thermodynamic model as used herein (cf. Figure 12a in Rose et al. (2008)). This result is consistent with our results showing that χ approaches 1 for the fastest drying rates (cf. Figures 6 and 7). In another set of experiments, Rose et al. (2008) dried the aqueous particles using a silica gel diffusion drier. In this case, the calibration results of the two salts were self-consistent using χ = 1.08 for the NaCl particles (cf. Figure 13 in Rose et al. (2008)). Although a straight calibration line was used by Rose et al. (2008) for this case, re-analysis of the data shows that the residuals of the data compared to the line form a curve, implying a maximum value in the shape factor akin to our results in Figure 6. For example, the point at 0.25% supersaturation (corresponding approximately to 50-nm NaCl particles) in Rose et al. (2008) is above the line, suggesting χ > 1.08, whereas the points toward lower and upper

end of the supersaturation ranges (corresponding approximately to 30- and 130-nm NaCl particles, respectively) lie below the line, suggesting $\chi < 1.08$. The trend therefore shows a maximum in χ at an intermediate diameter, which is consistent with our trend showing the dependence of χ on particle size (cf. Figure 6).

Kuwata and Kondo (2009) employed measurements of particle mobility diameter made with a DMA and of particle specific mass made by an aerosol particle mass analyzer (APM) to determine χ for 50- to 150-nm NaCl particles. Among runs, χ varied from 1.09 to 1.14 at the lower end of the size range. At the upper end, it varied from 1.04 to 1.10. TSI diffusion dryers were used, which we again estimate provided a drying rate of 30 to 60 RH s⁻¹. The results at the lower end of the size range investigated by Kuwata and Kondo (2009) can be compared to those at the upper end of our size range, and the agreement is good. Specifically, the values of 1.09 to 1.14 in Kuwata and Kondo (2009) can be compared to values of 1.05 to 1.15 shown in Figure 6 for 50- to 80-nm particles and drying rates of 29.7 ± 0.7 and 58.4 ± 0.9 RH s⁻¹.

A complication in the aforementioned studies that employ dessicant-based diffusion dryers is that the drying capability can change with time as the dessicant saturates (Zelenyuk et al., 2006). Differences among experimental runs have been attributed to aging of the dessicant (Zelenyuk et al., 2006; Kuwata and Kondo, 2009). In contrast, for the flow-tube setup employed in the experiments of the present study, the sheath flow extracting the water vapor was operated in continuous flow, representing a set-up of continuous renewal. Therefore, there was no influence of previous runs on a current set of measurements. This experimental approach is precise and reliable for consistent and known drying rates.

6. Conclusions

This study presented experimental results showing the dependence of the dynamic shape factor χ of sub-100 nm NaCl particles on drying rate and particle size. Values of χ were determined from the mobility diameter measured by a DMA and the critical supersaturation determined by CCN analysis. The drying rate was quantified and varied from 5.5 ± 0.9 to $101 \pm 3 \text{ RH s}^{-1}$ using a laminar aerosol flow tube having a dry sheath flow and a wet aerosol core flow. The results show that the dynamic shape factor of NaCl particles can vary from values representing nearly cubic to almost spherical particles. Specifically, depending on particle size and drying rate, the value of χ ranged from 1.02 to 1.26. The value of χ decreased with increasing drying rate. High rates of drying (i.e., $101 \pm 3 \text{ RH s}^{-1}$) caused rapid evaporation and crystallization, tending to favor spherical shape. Slow rates of drying (i.e., $5.5 \pm 0.9 \text{ RH s}^{-1}$) led to slower evaporation and crystallization, tending to favor cubic shapes. At fixed drying rate, particles having diameters of 35 to 40 nm had the highest χ values, which approached those theoretically expected for cubes. For both smaller and larger particles, the χ values decreased, eventually approaching values representing a spherical geometry. The dependence of χ on particle size can be attributed to the competing effects of the dominant characteristic times of particle-phase diffusion of water and diffusive movement of NaCl monomers, coupled to system size. The approach introduced herein for studying shape factors can allow the continued development of more detailed and quantitative understanding of the factors influencing the morphology of dried submicron particles.

Acknowledgments. This material is based upon work supported by the Office of Science (BER), U.S. Department of Energy, Grant No. DE-FG02-08ER64529. The particle images were

collected at the LeRoy Eyring Center for High Resolution Electron Microscopy within the Center for Solid State Science at Arizona State University. Zhe Wang was the recipient of a Chinese Government Scholarship for Postgraduates. E. Lewis was supported by the U. S. Department of Energy's Office of Science under Contract No. DE-AC02-98CH10886. We thank John Shilling and George Biskos for the valuable discussion and suggestions.

Supporting Information Available. Table S1: Tabulation of data shown in Figure 6. Figure S1: (A) Critical dry mobility diameter of activation for different temperature-gradient settings of the CCNC instrument and different aerosol drying rates. (B) Same data as top figure but y-axis is shown as the ratio of the critical dry mobility diameter at one drying rate to the diameter at the fastest drying rate. Figure S2: A comparison between the activation curves of NaCl and $(\text{NH}_4)_2\text{SO}_4$ particles as a check on the homogeneity of the dynamic shape factors of the NaCl particles. Figure S3: Experimental reproducibility of the measured NaCl dynamic shape factors.

References

- Abramzon, B., and Sirignano, W. A. (1989), Droplet vaporization model for spray combustion calculations, *International Journal of Heat and Mass Transfer*, 32: 1605-1618.
- Adamson, A. W., and Gast, A. P. (1997), *Physical Chemistry of Surfaces*, 6th ed., Wiley, New York.
- Allen, M. D., and Raabe, O. G. (1985), Slip correction measurements of spherical solid aerosol-particles in an improved millikan apparatus, *Aerosol Sci. Technol.*, 4: 269-286.
- Barbe-le Borgne, M., Boulaud, D., Madelaine, G., and Renoux, A. (1986), Experimental-determination of the dynamic shape factor of the primary sodium peroxide aerosol, *J. Aerosol Sci.*, 17: 79-86.
- Baron, P. A., Sorensen, C. M., and Brockmann, J. E. (2001), Chapter 23: Nonspherical Particle Measurements: Shape Factors, Fractals, and Fibers, in *Aerosol Measurement*, edited by Baron, P. A. and Willeke, K., Wiley, New York.
- Baron, P. A., and Willeke, K. (2001a), *Aerosol Measurement: Principles, Techniques, and Applications*, second ed., Wiley, New York.
- Baron, P. A., and Willeke, K. (2001b), Chapter 4: Gas and Particle Motion, in *Aerosol Measurement*, edited by Baron, P. A. and Willeke, K., Wiley, New York.
- Biskos, G., Malinowski, A., Russell, L. M., Buseck, P. R., and Martin, S. T. (2006a), Nanosize effect on the deliquescence and the efflorescence of sodium chloride particles, *Aerosol Sci. Technol.*, 40: 97-106.
- Biskos, G., Paulsen, D., Russell, L. M., Buseck, P. R., and Martin, S. T. (2006b), Prompt deliquescence and efflorescence of aerosol nanoparticles, *Atmos. Chem. Phys.*, 6: 4633-4642.
- Biskos, G., Russell, L. M., Buseck, P. R., and Martin, S. T. (2006c), Nanosize effect on the hygroscopic growth factor of aerosol particles, *Geophys. Res. Lett.*, 33: L07801.
- Brenn, G., Wiedemann, T., Rensink, D., Kastner, O., and Yarin, A. L. (2001), Modeling and experimental investigation of the morphology of spray dried particles, *Chemical Engineering & Technology*, 24: 1113-1116.
- Brockmann, J. E., and Rader, D. J. (1990), APS response to nonspherical particles and experimental-determination of dynamic shape factor, *Aerosol Sci. Technol.*, 13: 162-172.
- Charlesworth, D. H., and Marshall, W. R. (1960), Evaporation from drops containing dissolved solids, *AIChE J.*, 6: 9-23.
- Cheng, Y. S., Allen, M. D., Gallegos, D. P., Yeh, H. C., and Peterson, K. (1988), Drag force and slip correction of aggregate aerosols, *Aerosol Sci. Technol.*, 8: 199-214.
- Cussler, E. L. (1984), *Diffusion: Mass Transfer in Fluid Systems*, Cambridge University Press, Cambridge.
- Dahneke, B. (1973a), Slip correction factors for nonspherical bodies. I. Introduction and continuum flow, *Aerosol Sci.*, 4: 139-145.
- Dahneke, B. (1973b), Slip correction factors for nonspherical bodies. II. Free molecule regime, *Aerosol Sci.*, 4: 147-161.
- Dahneke, B. (1973c), Slip correction factors for nonspherical bodies. III. The form of the general law, *Aerosol Sci.*, 4: 163-170.
- Davies, C. N. (1979), Particle-fluid interaction, *J. Aerosol Sci.*, 10: 477-&.

- DeCarlo, P. F., Slowik, J. G., Worsnop, D. R., Davidovits, P., and Jimenez, J. L. (2004), Particle morphology and density characterization by combined mobility and aerodynamic diameter measurements. Part 1: Theory, *Aerosol Sci. Technol.*, 38: 1185-1205.
- Dick, W., Huang, P. F., and McMurry, P. H. (1995), Characterization of 0.02 μm to 1.0 μm particle losses in PermaPure dryers: Dependence on Size, Charge, and Relative Humidity (report 936), Particle Technology Laboratory, University of Minnesota.
- Dixkens, J., and Fissan, H. (1999), Development of an electrostatic precipitator for off-line particle analysis, *Aerosol Sci. Technol.*, 30: 438-453.
- Duffie, J. A., and Marshall, W. R. (1953), Factors Influencing the Properties of Spray-dried Materials, *Chemical Engineering Progress*, 49: 417-423.
- Hentschel, M. L., and Page, N. W. (2003), Selection of descriptors for particle shape characterization, *Particle & Particle Systems Characterization*, 20: 25-38.
- Katrib, Y., Martin, S. T., Rudich, Y., Davidovits, P., Jayne, J. T., and Worsnop, D. R. (2005), Density changes of aerosol particles as a result of chemical reaction, *Atmos. Chem. Phys.*, 5: 275-291.
- Kelly, W. P., and McMurry, P. H. (1992), Measurement of particle density by inertial classification of differential mobility analyzer generated monodisperse aerosols, *Aerosol Sci. Technol.*, 17: 199-212.
- King, S. M., Rosenoern, T., Shilling, J. E., Chen, Q., and Martin, S. T. (2007), Cloud condensation nucleus activity of secondary organic aerosol particles mixed with sulfate, *Geophys. Res. Lett.*, 34: L24806.
- Kittelson, D. B. (1998), Engines and nanoparticles: A review, *J. Aerosol Sci.*, 29: 575-588.
- Kodas, T. T., and Hampden-Smith, M. (1999), *Aerosol Processing of Materials*, Wiley, New York.
- Kousaka, Y., Endo, Y., Ichitsubo, H., and Alonso, M. (1996), Orientation-specific dynamic shape factors for doublets and triplets of spheres in the transition regime, *Aerosol Sci. Technol.*, 24: 36-44.
- Kramer, L., Poschl, U., and Niessner, R. (2000), Microstructural rearrangement of sodium chloride condensation aerosol particles on interaction with water vapor, *J. Aerosol Sci.*, 31: 673-685.
- Kreidenweis, S. M., Koehler, K., DeMott, P. J., Prenni, A. J., Carrico, C., and Ervens, B. (2005), Water activity and activation diameters from hygroscopicity data - Part I: Theory and application to inorganic salts, *Atmos. Chem. Phys.*, 5: 1357-1370.
- Kuwata, M., and Kondo, Y. (2009), Measurements of particle masses of inorganic salt particles for calibration of cloud condensation nuclei counters, *Atmos. Chem. Phys.*, 9: 5921-5932.
- Lance, S., Medina, J., Smith, J. N., and Nenes, A. (2006), Mapping the operation of the DMT Continuous Flow CCN counter, *Aerosol Sci. Technol.*, 40: 242-254.
- Leong, K. H. (1987), Morphology of aerosol-particles generated from the evaporation of solution drops - Theoretical considerations, *J. Aerosol Sci.*, 18: 511-524.
- Lewis, E. R., and Schwartz, S. E. (2004), Chapter 2. Fundamentals, in *Sea Salt Aerosol Production*, edited, American Geophysical Union, Washington, D.C., p. 61.
- Lewis, E. R. (2008), An examination of Kohler theory resulting in an accurate expression for the equilibrium radius ratio of a hygroscopic aerosol particle valid up to and including relative humidity 100%, *Journal of Geophysical Research-Atmospheres*, 113.
- Lin, J. C., and Gentry, J. W. (2003), Spray drying drop morphology: Experimental study, *Aerosol Sci. Technol.*, 37: 15-32.

- Liu, B. Y. H., and Lee, K. W. (1975), Aerosol generator of high stability, *Am. Ind. Hyg. Assoc. J.*, 36: 861-865.
- Mifflin, A. L., Smith, M. L., and Martin, S. T. (2009), Morphology hypothesized to influence aerosol particle deliquescence, *Phys. Chem. Chem. Phys.*, 11: 10095-10107.
- Mikhailov, E., Vlasenko, S., Niessner, R., and Poschl, U. (2004), Interaction of aerosol particles composed of protein and salts with water vapor: hygroscopic growth and microstructural rearrangement, *Atmos. Chem. Phys.*, 4: 323-350.
- Mikhailov, E., Vlasenko, S., Martin, S. T., Koop, T., and Poschl, U. (2009), Amorphous and crystalline aerosol particles interacting with water vapor: conceptual framework and experimental evidence for restructuring, phase transitions and kinetic limitations, *Atmos. Chem. Phys.*, 9: 9491-9522.
- Park, K., Kittelson, D. B., and McMurry, P. H. (2004), Structural properties of diesel exhaust particles measured by transmission electron microscopy (TEM): Relationships to particle mass and mobility, *Aerosol Sci. Technol.*, 38: 881-889.
- Petters, M. D., Prenni, A. J., Kreidenweis, S. M., and DeMott, P. J. (2007), On measuring the critical diameter of cloud condensation nuclei using mobility selected aerosol, *Aerosol Sci. Technol.*, 41: 907-913.
- Roberts, G. C., and Nenes, A. (2005), A continuous-flow streamwise thermal-gradient CCN chamber for atmospheric measurements, *Aerosol Sci. Technol.*, 39: 206-221.
- Rose, D., Gunthe, S. S., Mikhailov, E., Frank, G. P., Dusek, U., Andreae, M. O., and Poschl, U. (2008), Calibration and measurement uncertainties of a continuous-flow cloud condensation nuclei counter (DMT-CCNC): CCN activation of ammonium sulfate and sodium chloride aerosol particles in theory and experiment, *Atmos. Chem. Phys.*, 8: 1153-1179.
- Shilling, J. E., King, S. M., Mochida, M., and Martin, S. T. (2007), Mass spectral evidence that small changes in composition caused by oxidative aging processes alter aerosol CCN properties, *J. Phys. Chem.*, 111: 3358-3368.
- Slowik, J. G., Stankin, K., Davidovits, P., Williams, L. R., Jayne, J. T., Kolb, C. E., Worsnop, D. R., Rudich, Y., DeCarlo, P. F., and Jimenez, J. L. (2004), Particle morphology and density characterization by combined mobility and aerodynamic diameter measurements. Part 2: Application to combustion-generated soot aerosols as a function of fuel equivalence ratio, *Aerosol Sci. Technol.*, 38: 1206-1222.
- Slowik, J. G., Cross, E. S., Han, J. H., Kolucki, J., Davidovits, P., Williams, L. R., Onasch, T. B., Jayne, J. T., Kolb, C. E., and Worsnop, D. R. (2007), Measurements of morphology changes of fractal soot particles using coating and denuding experiments: Implications for optical absorption and atmospheric lifetime, *Aerosol Sci. Technol.*, 41: 734-750.
- Walton, D. E. (2000), The morphology of spray-dried particles a qualitative view, *Drying Technology*, 18: 1943-1986.
- Wise, M. E., Biskos, G., Martin, S. T., Russell, L. M., and Buseck, P. R. (2005), Phase transitions of single salt particles studied using a transmission electron microscope with an environmental cell, *Aerosol Sci. Technol.*, 39: 849-856.
- Yun, X., and Kodas, T. T. (1993), Droplet evaporation and solute precipitation during spray-pyrolysis, *J. Aerosol Sci.*, 24: 893-908.
- Zelenyuk, A., Cai, Y., and Imre, D. (2006), From agglomerates of spheres to irregularly shaped particles: Determination of dynamic shape factors from measurements of mobility and vacuum aerodynamic diameters, *Aerosol Sci. Technol.*, 40: 197-217.

List of Tables

- Table 1.** Coefficients of $m_p^{dry}[S_c]$ for equation 2 that parameterize the dependence of dry particle mass m_p^{dry} (kg) on critical supersaturation S_c (%) for sodium chloride and ammonium sulfate at 298 K and 304 K. For S_c ranging from 0.1 to 2.0%, the parameterization describes m_p^{dry} within a multiplicative factor of 1.003 compared to the original equation (i.e., equation 1). The AP3 model of Rose et al. (2008) was used to generate the primary data used in the parameterization.
- Table 2.** Calculated drying rates in the laminar-flow tube for experimental conditions 1 to 4 employed in this study. The initial aerosol RH (i.e., core flow) and the initial sheath RH (i.e., outer flow) of each experimental condition are shown. The final column shows the calculated average drying rate at an aerosol RH of 45% (i.e., the efflorescence RH of NaCl particles; cf. equation 8). The drying rates are shown as open circles in panel D of Figure 2.
- Table 3.** Calculated drying rates in the laminar-flow tube for model cases I to IV. Each case corresponds to an initial aerosol RH and an initial sheath RH. The model is described by equation 6. Calculations are carried out for three interaction times (i.e., corresponding to three longitudinal positions). Shown in the table are the modeled aerosol RH at each interaction time and the average drying rate at that aerosol RH (cf. equation 8). The cases listed in the table correspond to those plotted in panel C of Figure 2.
- Table 4.** Quantitative shape descriptors of aspect ratio, form factor, and roundness for the TEM images shown in Figure 3. The aspect ratio is the quotient of the minimum and maximum linear measurements. The form factor (also known as circularity) is

calculated as $(4\pi \text{ Area} / \text{Perimeter}^2)$, where the *Area* and *Perimeter* are taken as appropriate pixel counts in the image. Roundness is defined as $((4 \text{ Area}) / (\pi \text{ maxLength}^2))$, where *maxLength* is the maximum linear measurement. A perfect circle yields a value of 1.0 for each descriptor. Definitions of “slow” and “fast” drying are as described for Figure 3.

Table 5. Summary of the dynamic shape factors reported in the literature and those measured in this study for NaCl particles.

List of Figures

Figure 1. Schematic diagram of the experimental apparatus. (A) Aerosol generation by atomization, adjustment of aerosol RH in Nafion 1 to high RH, drying of aerosol RH in the laminar-flow tube (see also panel B), selection of particle mobility diameter by nDMA, and measurement of activated CCN fraction. (B) Illustration of the drying of the aerosol flow by radial water-vapor diffusion into the sheath flow and the subsequent crystallization of the particles in the aerosol flow. The circles with solid dots represent spherical solution drops in a humid core flow, and the solid cubes represent the crystallized particles in a core flow. The dynamic shape factor of these cubes depends on the drying rate. Key: CCNC, cloud condensation nucleus counter; CPC, condensation particle counter; nDMA, nano differential mobility analyzer; MFC, mass flow controllers; PID, proportional integral derivative controller; PT, pressure transducer; RHS, relative humidity sensor.

Figure 2. Drying rate. (A) Depiction of the RH profiles in the inner and outer flows along the longitudinal axis of the flow tube. Flow is from left to right. The lighter solid lines represent the cross section of RH profile along the interaction distance and the dashed lines show the interaction area for inner and outer flows. (B) Depiction of a volume element for calculating the drying rate in the aerosol flow. (C) Calculated RH in the aerosol flow for increasing interaction time. Results are shown for the four model cases specified in Table 3. The interaction time can be related to the longitudinal position z in the flow tube by use of the linear flow velocity. The arrow indicates the ERH of NaCl particles (i.e., 45%). The slope of the curve at this point is the drying rate (RH s^{-1}) for an aerosol RH of 45%. (D) Drying rate (RH s^{-1}) at an aerosol RH of

45% for variable initial aerosol RH. Results are shown for several different initial ΔRH between the aerosol RH and the sheath RH. Lines show the ranges of drying rates that can be obtained by varying the initial RH but holding constant initial ΔRH . The solid triangles correspond to the four model case listed in Table 3, and the open circles indicate the calculated drying rates for the experimental conditions listed in Table 2.

Figure 3. Transmission electron micrographs for NaCl particles prepared at different drying rates. Images are shown for particles collected by DMA classification at 25-, 40-, and 65-nm dry mobility diameter (+1 charge). Slow and fast drying refers to experiments 1 and 4 of Table 2 (i.e., 5.5 ± 0.9 and $101 \pm 3 \text{ RH s}^{-1}$, respectively). Images within one diameter classification are on the same scale; images between diameter classifications are scaled for a common display size. Quantitative descriptors of the images are provided in Table 4.

Figure 4. CCN activation curves at 0.5% supersaturation for NaCl particles prepared using four drying rates (cf. Table 2). The lines passing through the data are sigmoidal fits. The mobility-equivalent critical diameter is the intersection of a fit curve with the dashed line drawn at an activated fraction of 0.5. For comparison, the mass-equivalent critical diameter of a NaCl particle active at 0.5% supersaturation is 35.7 nm. Indicated by arrows are the mobility-equivalent critical diameters expected for NaCl particles having dynamic shape factors χ of 1.00, 1.08, and 1.24.

Figure 5. CCN activation curves for supersaturations ranging from 0.15 to 1.0%. The drying rate is held constant at $29.7 \pm 0.7 \text{ RH s}^{-1}$. For orientation, the thick line in this figure is the same as shown in Figure 4.

Figure 6. (A) Dynamic shape factors χ of NaCl particles having dry mobility diameters from 23 to 84 nm and prepared by drying rates ranging from 5.5 ± 0.9 to 101 ± 3 RH s⁻¹ (cf. Table 2). (B) Same as panel A but plotted as the inferred aqueous diameter prior to drying (i.e., by obtaining m_p^{dry} from S_c and then d_{ve}^{aq} from m_p^{dry} for the initial RH values of Table 2). Uncertainty is based on the standard deviation of repeated measurements made on different days for nominally identical conditions (cf. Figure S3). Lines show the expected shape factors χ_c , χ_{fm} , and χ_t of cubes in the continuum, free-molecule, and transition regimes, respectively (DeCarlo et al., 2004; Biskos et al., 2006c). For orientation, the arrow marks the data point corresponding to the thick line shown in Figures 4 and 5.

Figure 7. Dynamic shape factors χ of NaCl particles for increasing drying rate. Results are shown for particles having mass-equivalent diameters ranging from 22.7 to 65.2 nm. The lines are not model fits but are drawn to aid the eye. Uncertainty on the data points is as described for Figure 6. For orientation, the arrow marks the data point corresponding to the thick line shown in Figures 4 and 5.

Parameter	NaCl		(NH ₄) ₂ SO ₄	
	298 K	304 K	298 K	304 K
c_0	$1.181 \cdot 10^{-20}$	$1.112 \cdot 10^{-20}$	$2.253 \cdot 10^{-20}$	$2.122 \cdot 10^{-20}$
c_1	0.1182	0.1193	0.1184	0.1197
c_2	-0.0249	-0.0256	-0.0261	-0.0269

Table 1.

Experiment	Experimental Conditions			Calculated
	Initial Aerosol RH (%)	Initial Sheath RH (%)	Initial Δ RH (%)	$RH'_{ERH=45\%}$ (RH s ⁻¹)
1	57.2 ± 0.5	39.2 ± 1.0	18.0 ± 0.5	-5.5 ± 0.9
2	56.8 ± 0.8	27.6 ± 0.6	29.2 ± 0.3	-29.7 ± 0.7
3	57.5 ± 0.9	16.0 ± 0.4	41.5 ± 0.5	-58.4 ± 0.9
4	56.5 ± 1.1	6.4 ± 0.2	50.1 ± 0.8	-101 ± 3

Table 2.

Case	Model Conditions			Interaction Time (s)	Longitudinal position (m)	Model Results			
	Initial Aerosol RH (%)	Initial Sheath RH (%)	Initial Δ RH (%)			Aerosol RH (%)	Sheath RH (%)	Δ RH (%)	$(\frac{dRH}{dt})_{Aerosol\ RH}$ (RH s ⁻¹)
I	60	40	20	0	0	60.0	40.0	20.0	-8.5×10^6
				0.96	0.121	45.0	41.0	4.0	-3.8
				7.94	1.000	41.3	41.3	0	0
II	70	30	40	0	0	70.0	30.0	40.0	-1.71×10^7
				0.52	0.066	45.0	31.7	13.3	-16.6
				7.94	1.000	32.7	32.7	0	0
III	80	20	60	0	0	80.0	20.0	60.0	-2.56×10^7
				0.43	0.054	45.0	22.4	22.6	-30.4
				7.94	1.000	24.0	24.0	0	0
IV	90	10	80	0	0	90.0	10.0	80.0	-3.42×10^7
				0.39	0.049	45.0	13.1	31.9	-44.5
				7.94	1.000	15.4	15.3	0.1	-0.05

Table 3.

Diameter (nm)	Drying condition	Aspect ratio	Form factor	Roundness
25	slow	0.88	0.86	0.93
	fast	0.90	0.88	0.94
40	slow	0.85	0.84	0.91
	fast	0.87	0.87	0.93
65	slow	0.83	0.84	0.92
	fast	0.85	0.86	0.93

Table 4.

Diameter (nm)	Drying method	Shape factor	Source
120-560	Dried by diffusion dryer	1.08	Kelly and McMurry, 1992
96	Dried by diffusion dryer	1.03-1.17	Kramer et al., 2000
99	First dried by diffusion dryer, then hydrated and dried again by mixing with dry air (Ratio 10:1)	1.06	Mikhailov et al., 2004
201		1.07	
6-60	Dried by mixing with dry air ^a / Hydrated and then dried in a Nafion conditioner ^b	1.22- 1.24	Biskos et al., 2006c
100-300	First dried by two diffusion dryers and then by mixing with dry compressed air (Ratio 50:1)	1.02	Zelenyuk et al., 2006
200-800		1.06-1.17	
200-700	Dried by mixing with dry air (Ratio 50:1)	1.30-1.40	
25-160 ^c	Dried by mixing with dry air (Ratio 60~15:1)	1.00	Rose et al., 2008
30-130 ^c	Dried by diffusion dryer	1.08	
50-150	Dried by two diffusion dryers	1.05-1.14	Kuwata and Kondo, 2009
23-84	Dried in flow tube with controlled and quantified drying rate of $5.5 \pm 0.9 \text{ RH s}^{-1}$	1.12-1.26 ^d	This study
	of $29.7 \pm 0.7 \text{ RH s}^{-1}$	1.05-1.18	
	of $58.4 \pm 0.9 \text{ RH s}^{-1}$	1.07-1.15	
	of $101 \pm 3 \text{ RH s}^{-1}$	1.02-1.11	

^a Particles generated by electrospray

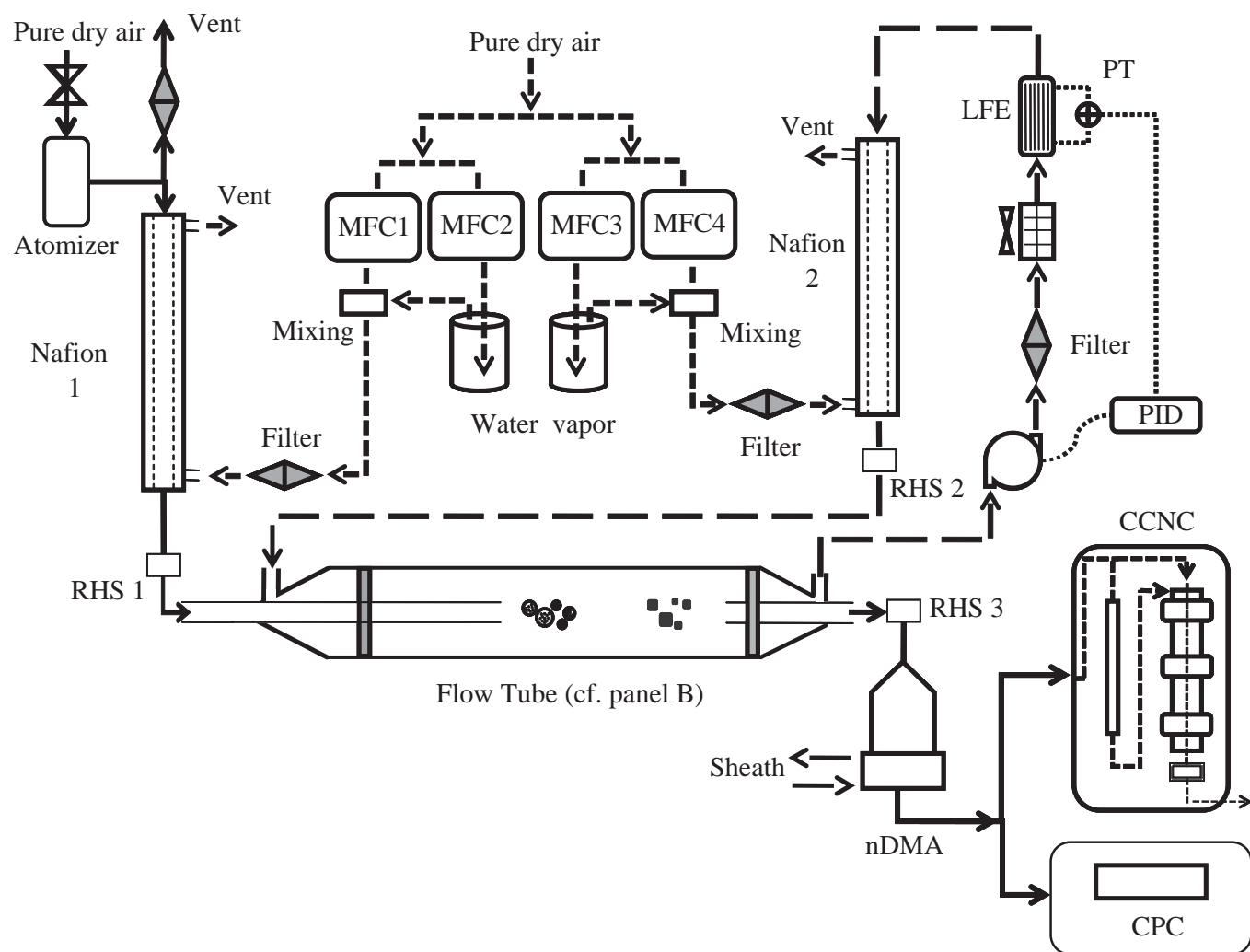
^b Particles generated by vaporization-condensation

^c Diameters were approximately calculated from associated supersaturation in Rose et al., 2008

^d Range of values arises from the size dependence investigated from 23 to 84 nm

Table 5.

A



B

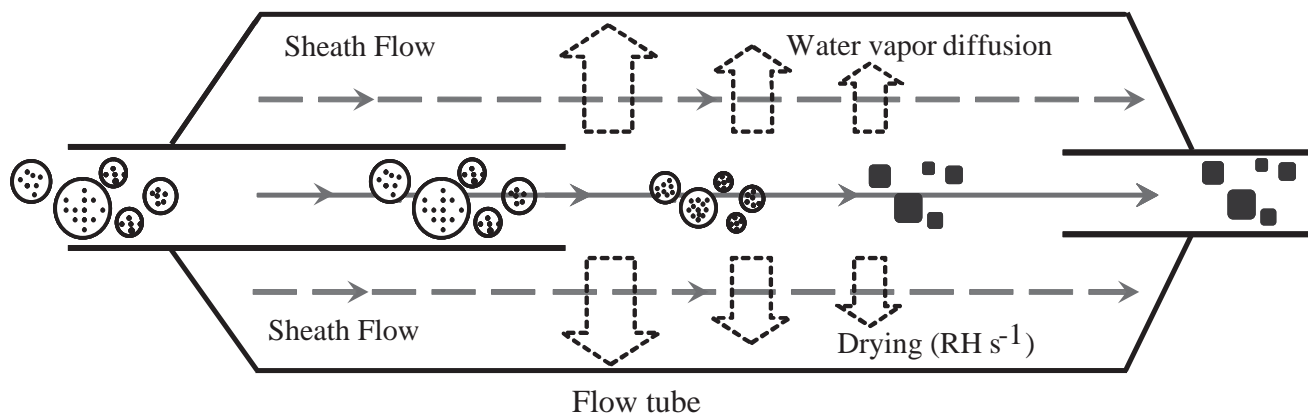


Figure 1.

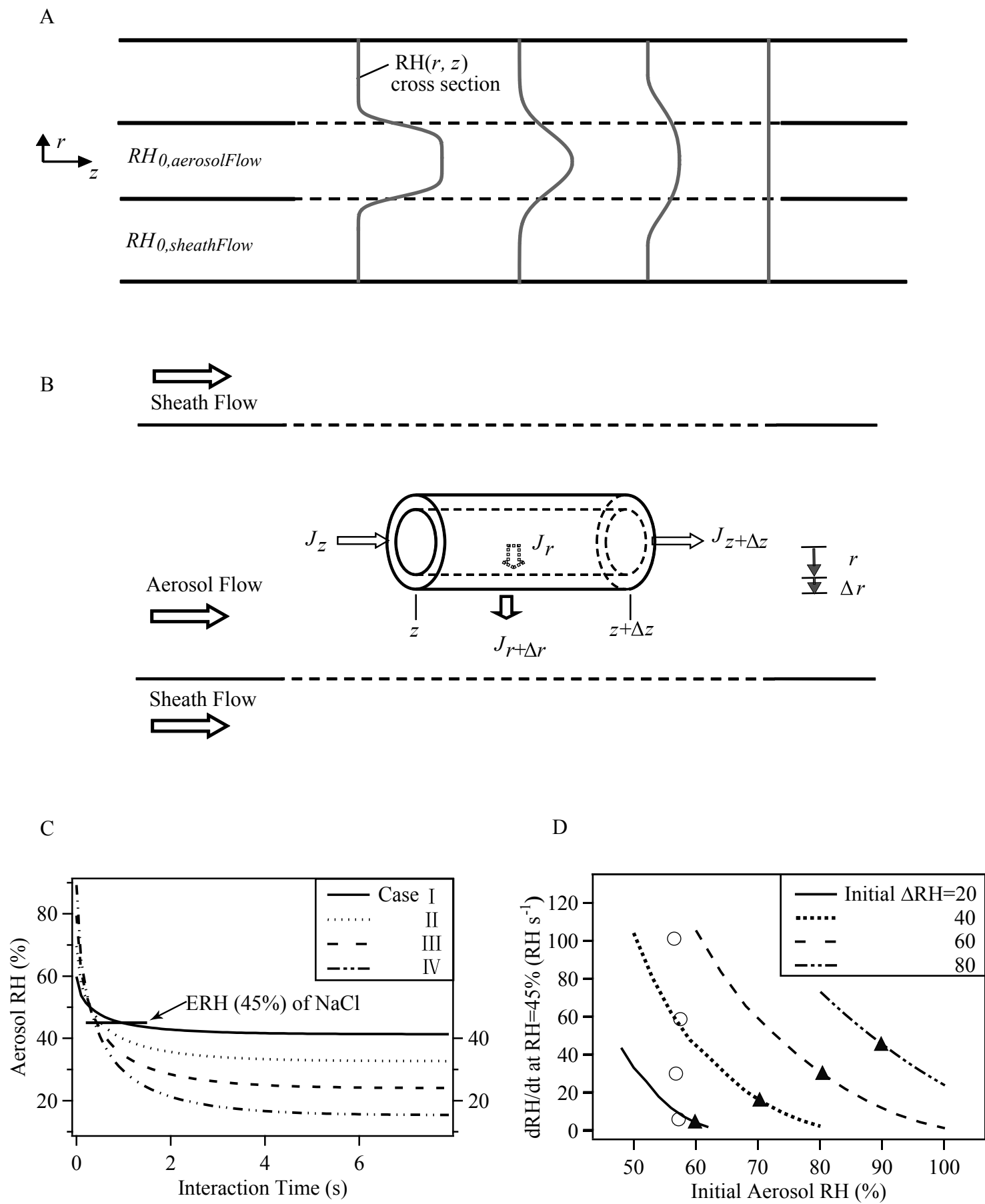


Figure 2.

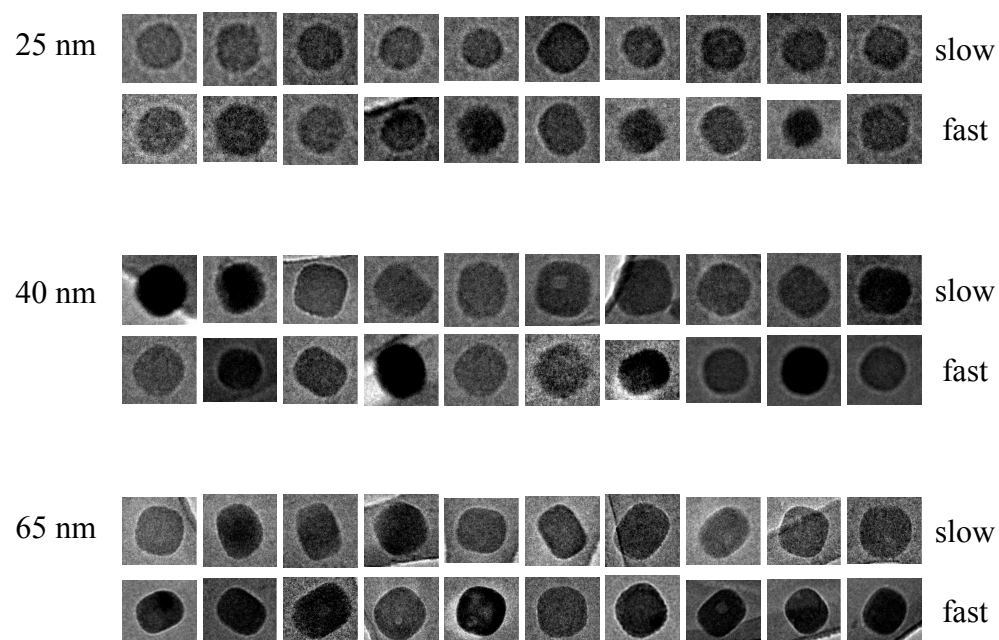


Figure 3.

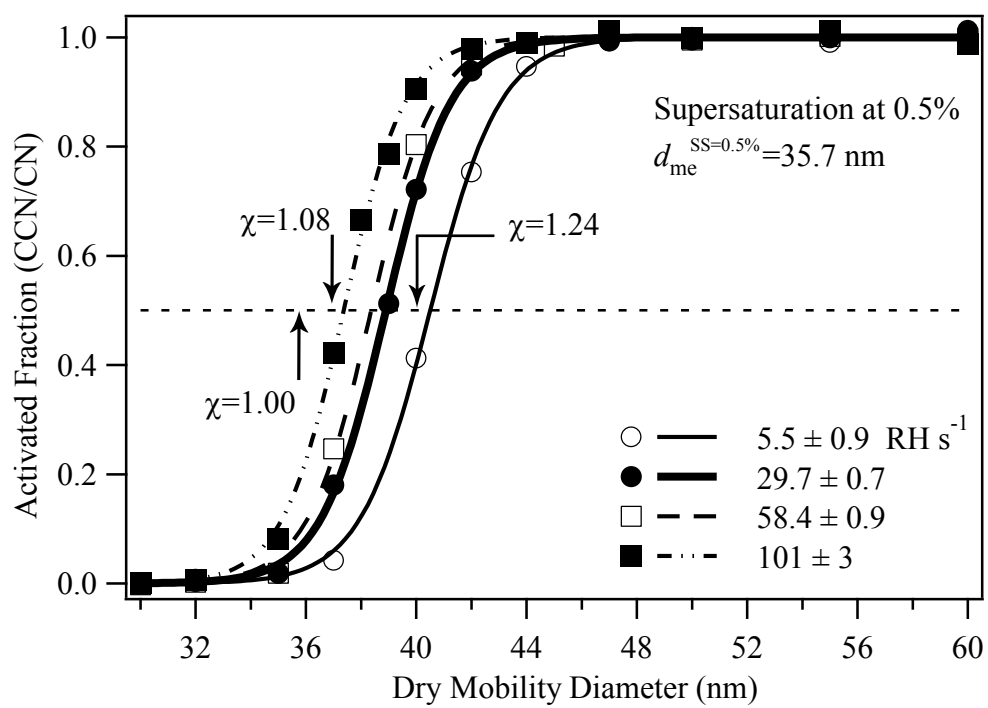


Figure 4.

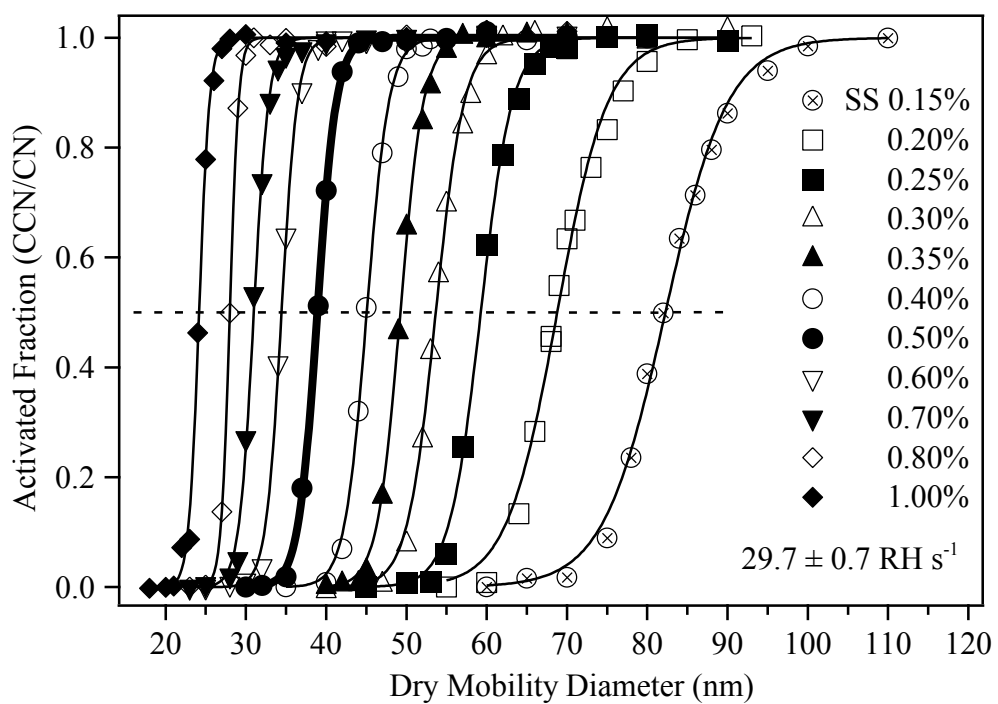


Figure 5.

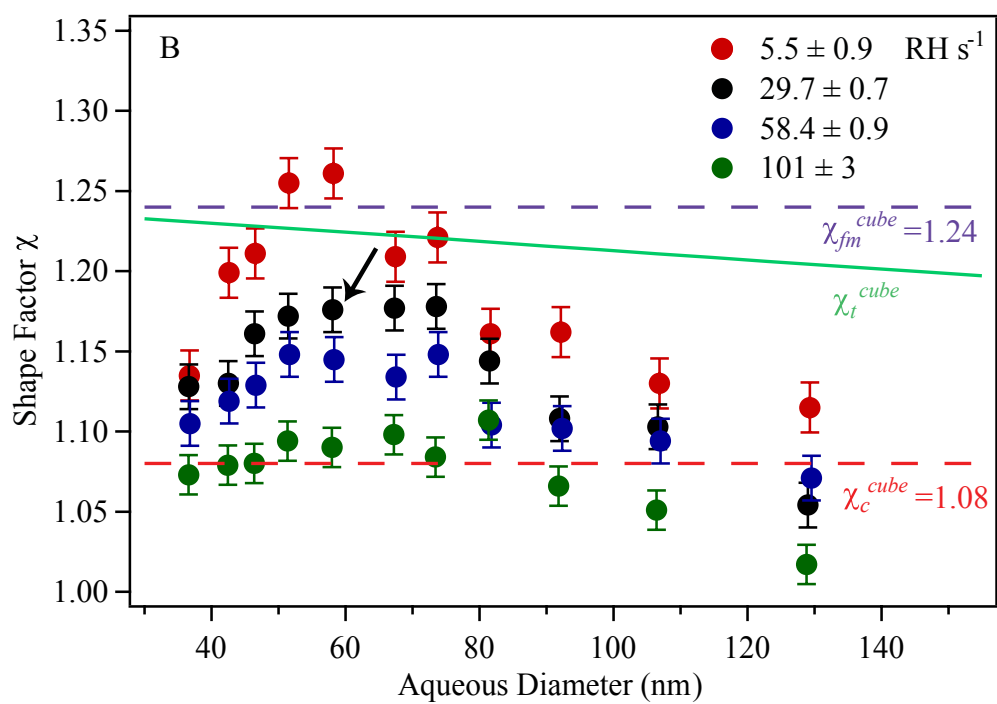
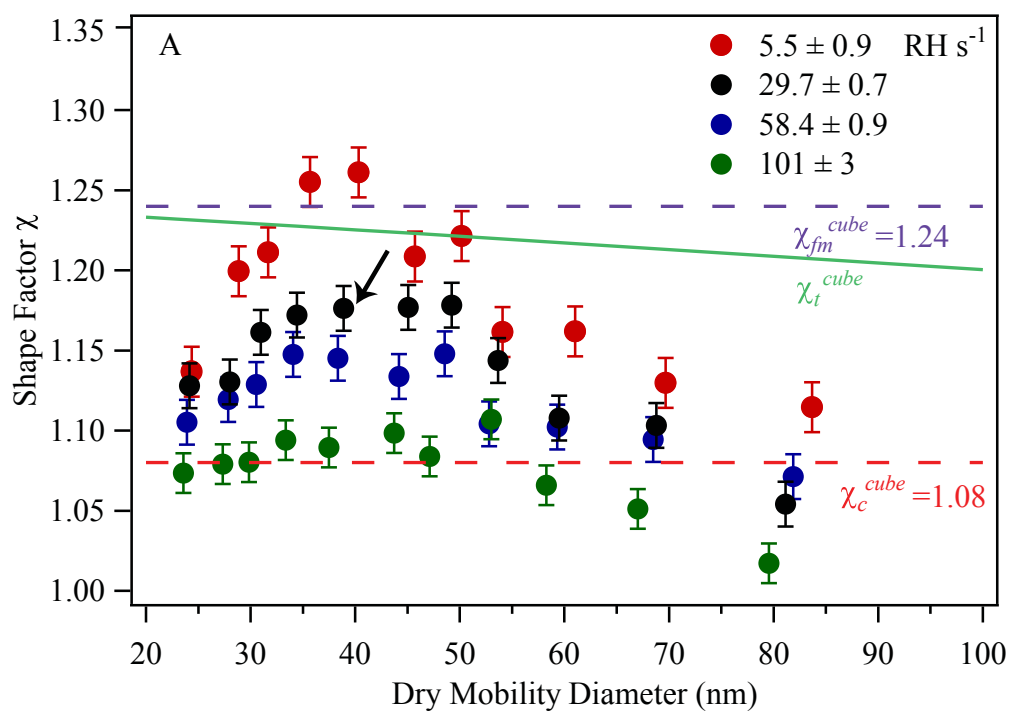


Figure 6.

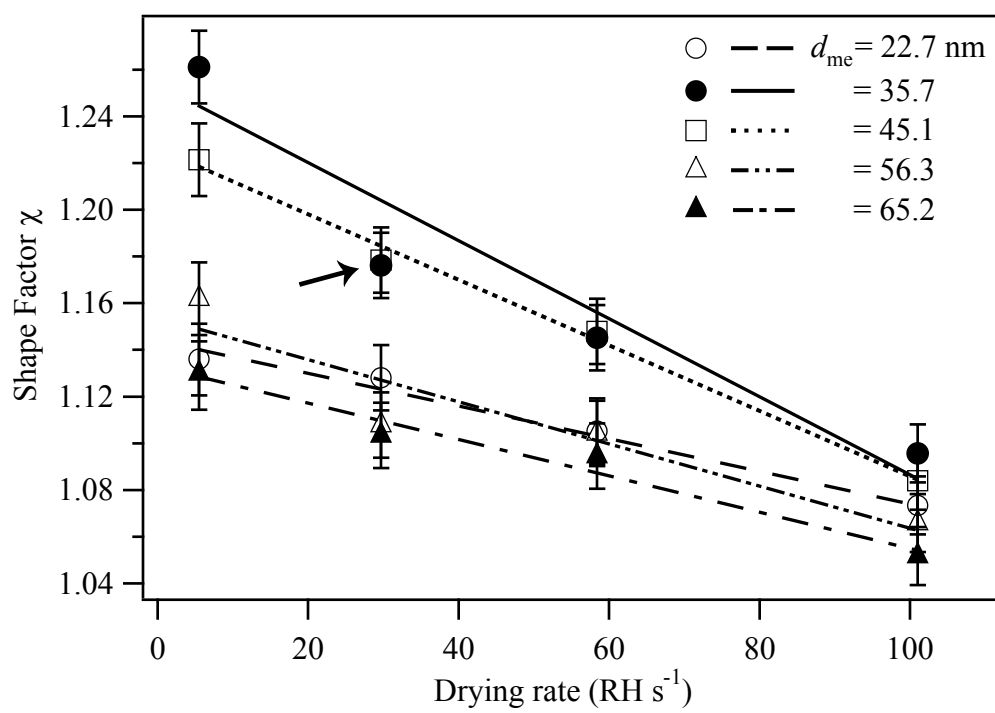


Figure 7.

List of Supplementary Material

Table S1. Measured dynamic shape factors χ of NaCl particles having dry mobility diameters from 23 to 84 nm and corresponding initial aqueous diameters from 36 to 130 nm, for all quantified drying rates.

Figure S1. (A) Critical dry mobility diameter of activation for different temperature-gradient settings (i.e., corresponding to supersaturation of 0.15 to 1.0%) of the CCNC instrument and different aerosol drying rates. (B) Same data as top figure but y-axis is shown as the ratio of the critical dry mobility diameter at one drying rate to the diameter at the fastest drying rate (i.e., $101 \pm 3 \text{ RH s}^{-1}$).

Figure S2. Comparison of the CCN activation curves of NaCl particles at supersaturation of 0.35 and 0.5% and $(\text{NH}_4)_2\text{SO}_4$ particles at supersaturation of 0.5%. The lines represent sigmoidal fits of the data. The NaCl particles were prepared using a drying rate of $29.7 \pm 0.7 \text{ RH s}^{-1}$ at 298 K. The comparison is made as a check on the homogeneity of χ of a batch NaCl particles produced in each measurement. Since small $(\text{NH}_4)_2\text{SO}_4$ particles are nearly spherical for a range of drying conditions, we assume that the particles shape is almost identical in each measurement, and therefore the derived χ of $(\text{NH}_4)_2\text{SO}_4$ particles from each CCN activation curve should have unity. The spread of the CCN activation curve is mainly due to the limit of DMA transfer function. Similar narrow CCN activation curves with steep slope are found for NaCl comparing to $(\text{NH}_4)_2\text{SO}_4$, suggesting the similar unitive particle shape and consequently unitive χ for NaCl particles in each measurement. The good agreement of the curve shape between different salts also supports the validity of the experimental results.

Figure S3. Reproducibility of the determination of the dynamic shape factor. The points clustered near a single diameter (i.e., typically three but sometimes two points) represent repeat measurements made on different days for nominally identical conditions. Results are shown for two different drying rates. The solid lines are not model fits but are drawn to aid the eye.

Drying Rate (RH s ⁻¹)	Aqueous Diameter (nm)	Dry Mobility Diameter (nm)	Shape Factor
-5.5 ± 0.9	129.33	83.69	1.115
	106.87	69.68	1.130
	92.17	61.04	1.162
	81.67	54.09	1.161
	73.73	50.18	1.221
	67.48	45.70	1.209
	58.19	40.34	1.261
	51.55	35.69	1.255
	46.53	31.67	1.211
	42.58	28.87	1.199
	36.70	24.38	1.135
-29.7 ± 0.7	129.04	81.13	1.054
	106.62	68.78	1.103
	91.96	59.48	1.108
	81.48	53.65	1.144
	73.56	49.24	1.178
	67.33	45.06	1.177
	58.06	38.90	1.176
	51.44	34.44	1.172
	46.43	30.99	1.161
	42.48	28.00	1.130
	36.62	24.17	1.128
-58.4 ± 0.9	129.56	81.87	1.071
	107.05	68.48	1.094
	92.33	59.32	1.102
	81.81	52.80	1.104
	73.85	48.56	1.148
	67.59	44.18	1.134
	58.29	38.36	1.145
	51.64	34.07	1.148
	46.61	30.53	1.129
	42.65	27.86	1.119
	36.76	23.92	1.105
-101 ± 3	128.82	79.54	1.017
	106.44	67.01	1.051
	91.80	58.26	1.066
	81.35	53.01	1.107
	73.44	47.11	1.084
	67.21	43.71	1.098
	57.96	37.48	1.090
	51.35	33.36	1.094
	46.36	29.85	1.080
	42.42	27.33	1.079
	36.56	23.56	1.073

Tabel S1.

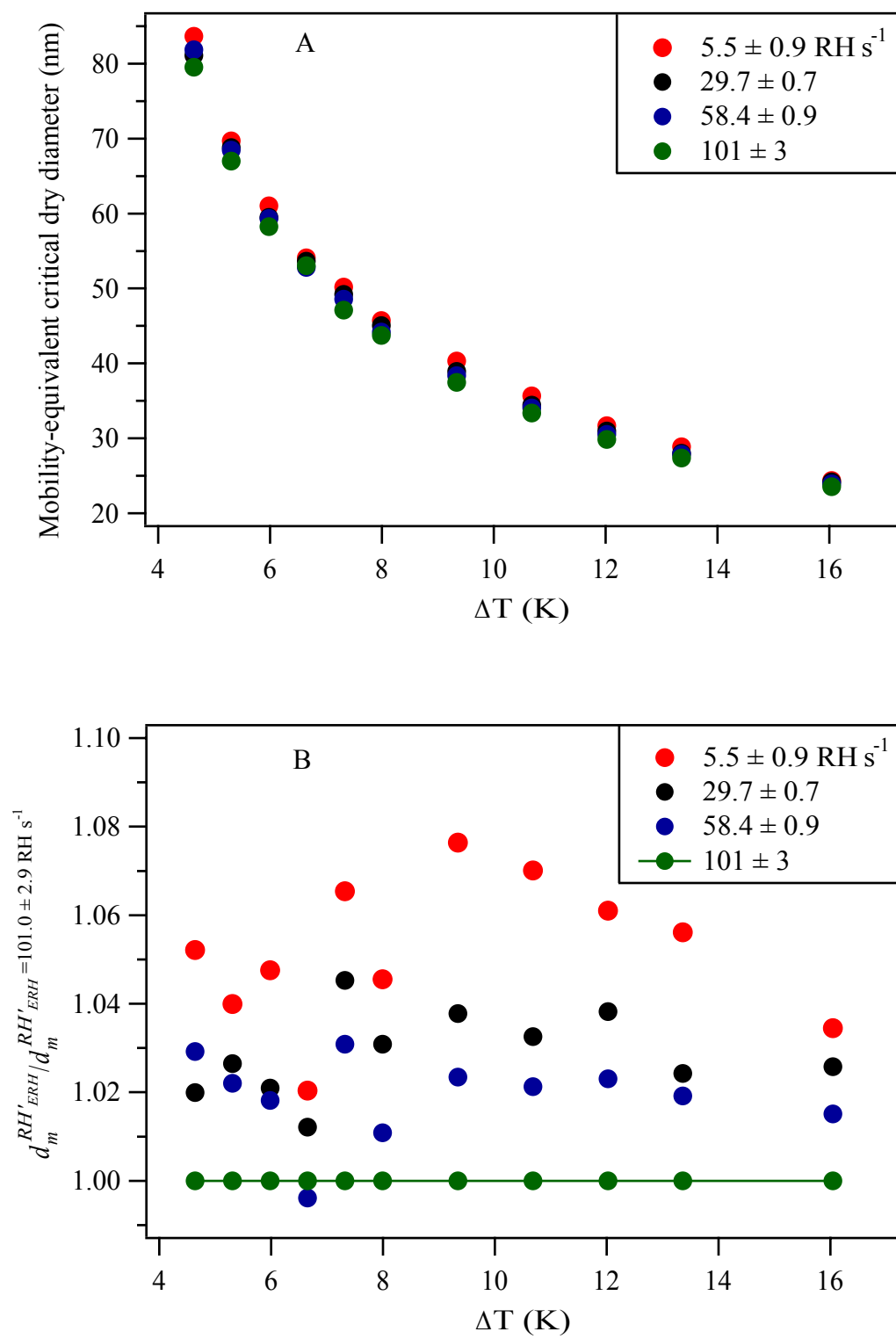


Figure S1.

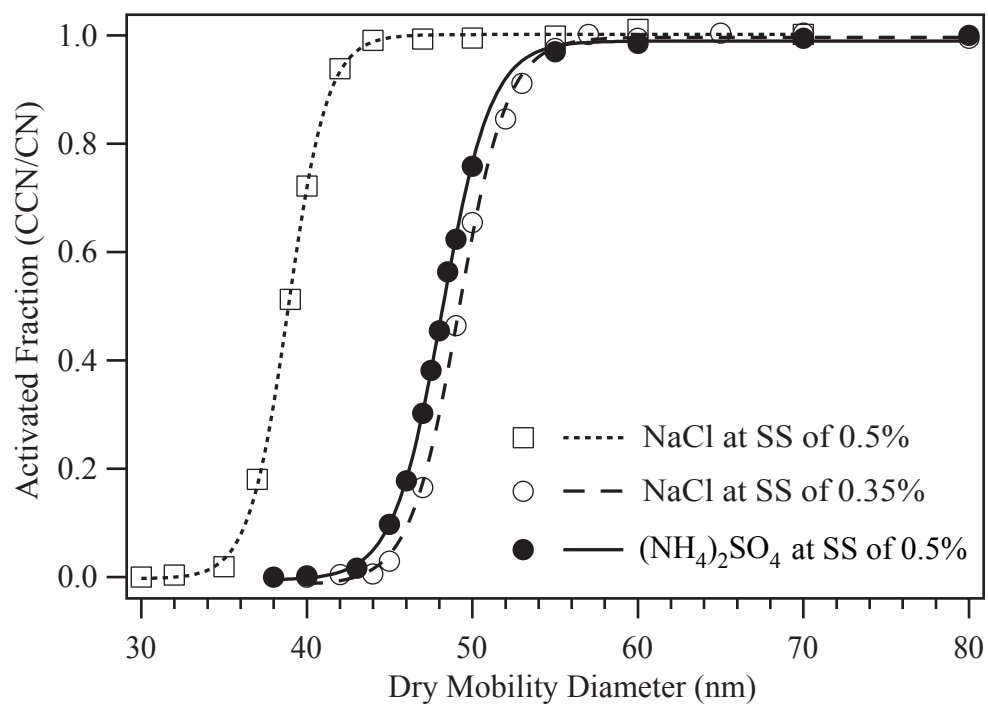


Figure S2.

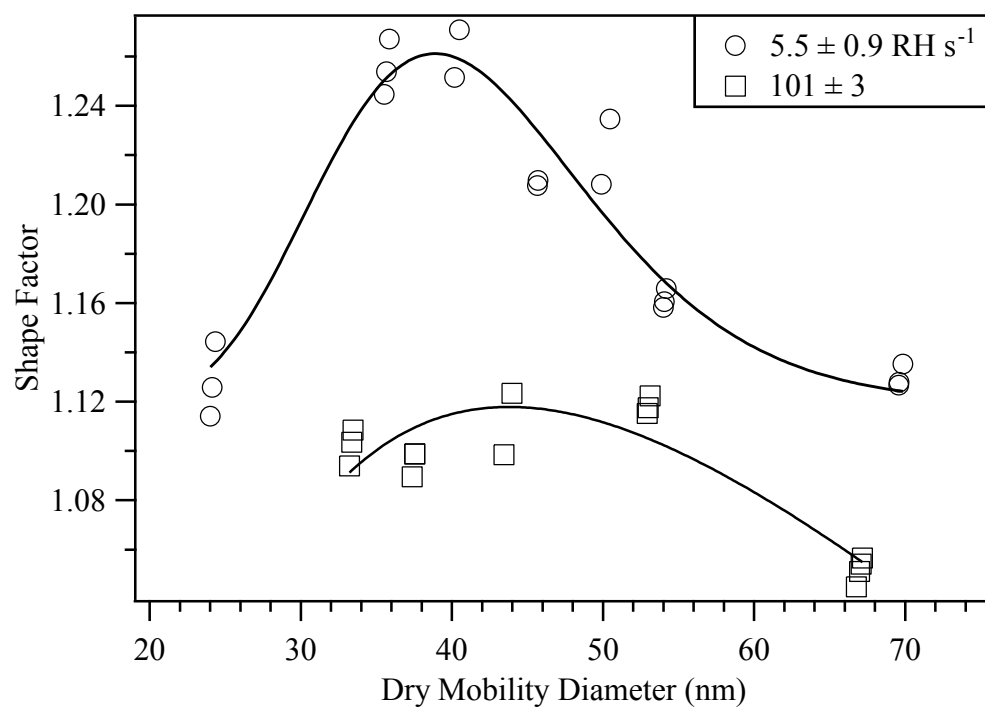


Figure S3.